LITHOS 400–401 (2021) 106424

Contents lists available at ScienceDirect

LITHOS

journal homepage: www.elsevier.com/locate/lithos

Research Article

Episodic recycling of ancient metasomatized continental lithosphere: Evidence from lower oceanic crust of the Central Indian Ridge

Abhishek Saha [a,*], Arghya Hazra [a,b], M. Santosh [c,d], Sohini Ganguly [b], Shan-Shan Li [c], C. Manikyamba [e]

[a] CSIR-National Institute of Oceanography, Dona Paula, Goa 403 004, India
[b] School of Earth, Ocean and Atmospheric Sciences, Goa University, Taleigão Plateau, Goa 403 206, India
[c] School of Earth Science and Resources, China University of Geosciences, Beijing 100 083, PR China
[d] Department of Earth Sciences, University of Adelaide, Adelaide SA 5005, Australia
[e] CSIR-Geophysical Research Institute, Uppal Road, Hyderabad 500 007, India

ARTICLE INFO

Keywords:
Indian Ocean
Central Indian Ridge
Upper mantle heterogeneity
Zircon U—Pb age
Continental Recycling

ABSTRACT

The tectonic and magmatic processes contributing to the heterogeneous nature of the upper mantle posit important constraints on the composition and differentiation of the Earth at various scales. Mid-oceanic ridges of intermediate, slow and very-slow spreading rates across the world's oceans are characterized by different crustal configurations portraying the compositional diversity of the upper mantle. The two viable processes that are attributed to chemical and isotopic heterogeneity of the mantle are: (i) multiple episodes of melt replenishment and melt-rock interaction in open magma systems; and (ii) recycling of oceanic and continental crustal materials and components of sub-continental lithospheric mantle. Here we present petrological, geochemical and zircon U—Pb geochronology data for the lower crustal oceanic gabbros from the Central Indian Ridge (CIR) of the Indian Ocean. This study presents continental (2525 Ma–173 Ma) zircons from the lower oceanic crust gabbros of the Central Indian Ridge and invokes Indian Ocean MOR mantle heterogeneity through episodic entrainment of ancient continental lithosphere of Madagascan and Gondwana origin prior to Indian Ocean opening. The geochemical features show a marked deviation from typical depleted N-MORB compositions and conform to an E-MORB affinity, which might suggest enriched lithospheric input into the depleted asthenospheric mantle. The transitional depleted to enriched mantle signature substantiates the role of lithosphere-asthenosphere interaction contributing towards accretion of lower oceanic crust gabbros beneath the CIR. The HFSE and REE compositions can be translated in terms of melt extraction by shallow level melting of a chemically heterogeneous upper mantle carrying depleted asthenospheric and recycled lithospheric components. Zircon U—Pb geochronology reveals a wide spectrum of ages ranging from 2525 Ma to 173 Ma suggesting multiple episodes of recycling of older crust into asthenospheric mantle. The continental inheritance of the dated zircon grains can be interpreted to represent trapped relics of older continental lithosphere into the Indian Ocean MOR mantle. Our results envisage delamination and recycling of older continental lithosphere into mantle asthenosphere (i) during the Mozambique ocean closure and Gondwana amalgamation at around 750 Ma, and (ii) in response to the dispersal of Gondwanaland at ~167 Ma ensued by opening of the Indian Ocean.

1. Introduction

The Earth's mantle preserves records of 4.56 Ga evolutionary history in terms of chemical differentiation, melt extraction, its migration and percolation, continental - oceanic fluxes, fluid circulation and crustal recycling. The pristine composition of the mantle-derived magmas, that could otherwise provide a first-order estimation of robust composition of the source/melting region, is modified by fractionation and assimilation of lower and upper crustal components en-route to the site of emplacement (Carlson and Ionov, 2019; Kaczmarek et al., 2008; Klein and Langmuir, 1987; Lambert et al., 2009). The accretion, composition and thickness (ACT) of juvenile oceanic crust at global mid-oceanic ridge-rift systems, comprising 60% of the Earth's surface area, are principally sustained by an interplay of several factors such as: (i)

* Corresponding author.
E-mail address: asaha@nio.org (A. Saha).

https://doi.org/10.1016/j.lithos.2021.106424
Received 26 April 2021; Received in revised form 6 August 2021; Accepted 12 August 2021
Available online 21 August 2021

spreading rates of diverging oceanic plates; (ii) thermal structure and composition of underlying mantle; (iii) partial melting of source mantle; (iv) mantle heterogeneity and metasomatism; (v) water content and oxidation state of mantle; (vi) magma differentiation and hybridization; (vii) magma intrusions and porous flow reactions between ascending melts, ambient mantle and lower oceanic crust; (viii) variable geometry, location and composition of axial magma chambers; and (ix) rate of supply of melt batches and on-axis conductive cooling (Coogan et al., 2000; Coogan and O'Hara, 2015; Leuthold et al., 2018; Lissenberg et al., 2013; Pagli et al., 2015). Mid-oceanic ridges (MOR) across the world's oceans are classified according to their full spreading rates as superfast (> 120 mm/yr), fast (80–120 mm/yr), intermediate (50–80 mm/yr), slow (20–50 mm/yr) and ultraslow (< 20 mm/yr; Karson et al., 2015). A typical 6.3 ± 0.9 km thick oceanic lithosphere, predominantly comprising abyssal peridotites, gabbro and basalt, is generated by adiabatic decompression melting of asthenospheric mantle beneath oceanic spreading centres at full spreading rates of 20 mm/year or above (White et al., 2001). The seafloor morphology and compositional architecture of oceanic lithosphere at intermediate to slow spreading ridges are controlled by widely variable styles of volcanism and plutonism. The oceanic lithosphere generated at intermediate to slow spreading ridges are characterized by decreased thickness, deeper axial rift valley and reduced magma supply collectively pointing to a fertile mantle underneath (Pagli et al., 2012, 2015). At slow spreading ridges, oceanic crust has been envisaged as a heterogeneous plum pudding comprising disseminated gabbro bodies within the peridotite with a capping of a thin layer of basalt (Ildefonse et al., 2007). Slow spreading ridges like MAR (Mid Atlantic Ridge) have magma storage in upper crustal chambers at >3 km depth. In contrast to a typical thickness of ~6 km, the oceanic crust at ultra-slow spreading ridges (<20 mm/yr) is relatively thinner owing to restricted melt supply and on-axis conductive cooling. It is characterized by deeper axial valleys, magma poor domains and localized volcanic centres separated by amagmatic segments and fed by shallow and restricted supply of melt derived from a heterogeneous mantle and transported through relatively thicker lithosphere (D'Errico et al., 2016; Dick et al., 2003). In case of intermediate to slow and ultraslow spreading ridges, a heterogeneous mantle character can be accounted in terms of co-existence of fertile and infertile mantle components where the enriched signatures are inherited from crustal recycling, infiltration and entrapment of melts from prior melting events.

The mid-oceanic ridges in the Indian Ocean are not continuous features, but are rather segmented and connected by transform or non-transform discontinuities. The fracture zones representing the transform discontinuities act as a tectonic window for providing access to lower crustal and uppermost mantle rocks. Therefore, focused and integrated petrological, geochemical and geochronological studies of ultramafic-mafic rocks recovered from different fracture zones of mid-oceanic ridges will yield important constraints on the geodynamic processes involved during the oceanic crustal accretion process in a ridge-transform system. In this paper, we present results from an integrated petrological, geochemical and zircon U—Pb geochronological study on the lower oceanic crust gabbros from the Central Indian Ridge (CIR), Indian Ocean. Based on the results, we evaluate their genesis, modes of crustal accretion, mantle source characters, role of recycled components and tectonic implications for Indian Ocean MOR mantle heterogeneity.

2. Geological setting

The Indian Ocean Ridge System (IORS) including Central Indian Ridge (CIR), Southwest and Southeast Indian Ridges (SWIR and SEIR) represents a magmatically and tectonically dynamic section of the global sub-ridge mantle system where juvenile oceanic crust is extracted at 10 to 200 km/Ma, from the mantle upwelling underneath in response to the divergence of existing oceanic lithospheric plates (Gale et al., 2014; Iyer and Ray, 2003). The IORS provides a potential corridor to constrain genesis, ascent, segregation, percolation, incubation and delivery (GASPID) of mantle derived melts to the crust that inherit distinct chemical signatures of a highly heterogeneous source. The CIR bifurcates at 25°30′S; 70°E at the Indian Ocean Triple Junction (IOTJ) in an apparently inverted Y shape to form SWIR and SEIR. The continuity of all these ridges is often offset by several NNE-SSW trending transform faults (also variously described as fracture zones), among which from north to south- Owen, Mahabiss, Sealark, Vityaz, Vema, Argo, Marie Celeste, Egeria and Gemino, Prince Edward, Indomed, Amsterdam, St. Paul- are of significance. CIR is the northern arm of the Indian Ocean Ridge System (IORS), and extends approximately from latitude 2°S to 25°30′S, and longitude from 62° to 67°E. At the Indian Ocean Triple Junction, the CIR bifurcates into two additional ridges as South East Indian Ridge (SEIR) and South West Indian Ridge (SWIR) (Ray et al., 2013). The CIR is a ca. 2550 km long linear chain of active submarine volcanoes and tectonic regimes, which is often displaced by numerous NNE-SSW trending transform faults and fractures zones (Hazra et al., 2021; Iyer and Ray, 2003; Mukhopadhyay et al., 2016). The CIR corresponds to a slow to intermediate spreading ridge (23–47 mm/yr), and seems to have attained its present geometry during the plate reorganisation as a result of the Indian subcontinent colliding with Asia (Dick et al., 2003; Radhakrishna and Verma, 2000; Ray et al., 2013; Saha et al., 2020). The time of formation of CIR is estimated to be ca. 38 Ma (Fisk et al., 1989; Patriat and Achache, 1984), or Late Cretaceous (Iyer and Ray, 2003). The interplay of tectonic and magmatic processes along the CIR significantly controls the processes of oceanic crust generation, its thickness, ocean floor and oceanic core complex (OCC) evolution (Lin and Morgan, 1992; Macdonald et al., 1988; Macdonald et al., 1991; Tolstoy et al., 1993).

Kamesh Raju et al. (1997) provided initial results of detailed segment scale investigations carried out over parts of the Central Indian Ridge using multibeam bathymetry (Fig. 1). The magnetic and bathymetric investigation results of Drolia et al. (2000) have provided tectonic implications of the ridge segmentation over a part of the Central Indian Ridge. Drolia and DeMets (2005) discussed the influence of diffuse plate deformation zone on the seafloor fabric and its implications, based on multibeam bathymetry and magnetic data. Subsequently, Kamesh Raju et al. (2012) studied the segmentation pattern of ~750 km long part of the Central Indian Ridge between 3°S and 11°S latitudes, using multibeam bathymetry and magnetic data. They documented distinct ridge-transform intersection (RTI) highs, representing oceanic core complexes / mega mullion structures that are observed at the less magmatic sections due to the predominance of tectonic extension.

3. Sampling and analytical techniques

The samples analysed in this study from the Central Indian Ridge were collected during an expedition of RV Sagar Kanya at Indian Ocean Ridge (SK 195). Dredging was carried out at 2 different locations (Fig. 1), selected on the basis of morphology and tectonic setting. Detailed description of the analytical methods is provided in Supplementary material.

4. Results

4.1. Petrography

The studied gabbro samples represent the lower crustal sequence beneath the Central Indian Ridge. These CIR gabbros are essentially composed of plagioclase, clinopyroxene and minor amount of orthopyroxene (Fig. 2A). In most of the samples, olivine is one of the important constituents which indicates early crystallization of magma at a high pressure in magma chamber as a product of partial melts generated at upper mantle. The olivine grains are relatively fresh but highly fractured (Fig. 2B). The gabbroic rocks show a typical layering due to early crystal segregation in the magma chamber in response to

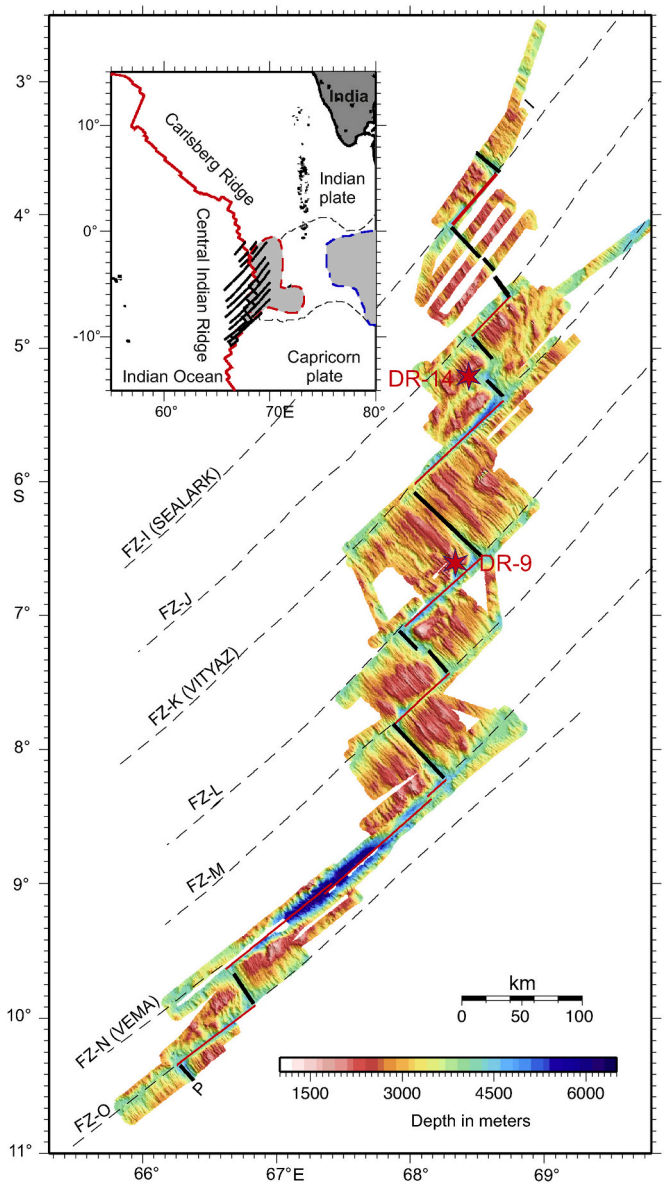

Fig. 1. Multibeam bathymetry map of the study area. The dredge locations are represented by red stars in the bathymetric map of the study area (modified after Kamesh Raju et al., 2012). Inset map shows the location of Central Indian Ridge in Indian Ocean Ridge System (IORS). (For interpretation of the references to colour in this figure legend, the reader is referred to the web version of this article.)

gravity settling (Fig. 2C). Overall, these rocks display cumulus texture where the cumulus phase is defined by calcic plagioclase [bytownite; An_{75-80} determined by symmetrical extinction angle (X^C)] and clinopyroxene (Cpx). Here the olivine represents the intercumulus residual melt composition (Fig. 2D). Olivine grains are altered along the grain boundaries and fractures (Figs.2B and D). Opaque oxides are also present in these gabbros (Fig. 2E). Under higher magnification, the Cpx grains show minor alteration along their cleavage traces. Another fine grained variety (microgabbro) also occurs in which the mineral grains are much finer than the layered gabbro. These rocks are composed of plagioclase, clinopyroxene, orthopyroxene and opaque oxides. In this variant, both ophitic and sub-ophitic textures are dominant (Fig. 2F). From the textural point of view, this rock might have formed at a shallower depth than the layered gabbro.

4.2. Geochemistry

4.2.1. Major elements

Major and trace element compositions of twelve submarine gabbro samples dredged from CIR are presented in Table 1. The studied samples are characterized by a restricted range of SiO_2 contents (41.05–48.55 wt %), low to moderate TiO_2 (0.14–1.45 wt%), moderate concentrations of $Fe_2O_3^{(T)}$ (5.78–12.05 wt%) with moderate to elevated abundances of Al_2O_3 (12.44–16.97 wt%), MgO (12.3–21.6 wt%) and CaO (). The Mg# and total alkali content for the samples range from 47 to 73 and 0.86–2.49 wt% respectively. The samples plot in the field of gabbro in the total alkali vs. silica (TAS) diagram (Fig. 3A). This observation is in accordance with the distinct tholeiitic nature of the studied samples on AFM ternary plot (Fig. 3B) of Irvine and Baragar (1971). The gabbros correspond to the abyssal tholeiite composition on FeO^T vs. FeO^T/MgO plot (Fig. 3C) and low K-tholeiite series in the K_2O vs. SiO_2 diagram (Fig. 3D).

4.2.2. Trace and rare earth elements

The transitional compatible trace element chemistry for the studied samples is marked by depleted Ni (25–73 ppm), Cr (58–843 ppm) and Co (21–86 ppm) concentrations with respect to primitive mantle values. Elevated abundance of Ni (399 ppm) and Cr (1904 ppm) is observed in one sample (Table 1). The rocks show variable total REE contents ranging from 1.4–52.23 ppm. Chondrite normalized REE patterns (Fig. 4A) for the gabbros show depleted to moderate enrichment in LREE and flat to fractionated HREE patterns with distinct positive Eu anomalies (Eu/Eu*:0.93–2.13). The $(La/Sm)_N$: 0.4–2.43, $(Ce/Yb)_N$: 0.4–1.43 and $(Gd/Yb)_N$: 0.73–1.13 collectively suggest depleted to discernible LREE/MREE, LREE/HREE and MREE/HREE fractionation patterns. Primitive mantle-normalized trace element abundance patterns (Fig. 4B) display distinct negative anomalies at Th, Nb, Zr, Hf with spikes at Ba thereby conforming to relative HFSE depletion and LILE enrichment for the studied samples.

4.2.3. Zircon morphology, U—Pb geochronology, REE chemistry, and Lu—Hf isotopes

4.2.3.1. SK-195-9-6. Zircons grains are rare and small in the gabbro, which are brownish in colour displaying prismatic to irregular shapes. They range in length from 30 to100 μm with aspect ratios of 2:1–1:1 (Fig. 5). Most of the grains display clear oscillatory zoning, and some of them show sector zoning. Few grains are surrounded by very thin bright rims.

Totally six spots were analysed from six zircons out of which two points were excluded from age calculations due to low concordance. The remaining four grains show a wide range of ages. The oldest grain yields Paleoproterozoic $^{207}Pb/^{206}Pb$ age of 2395 Ma (Table 2), with Th and U contents of 100 ppm and 211 ppm (Table 2) respectively. The Th/U ratio is 0.48, representing magmatic origin. The other three grains display $^{206}Pb/^{238}U$ ages of 349 Ma, 173 Ma, 140 Ma with Th and U contents in the range of 166–320 ppm, 232–333 ppm, and Th/U ratios of 0.72–1.1 (Table 2).

The REE contents of the analysed zircons show a wide range of 466–1054 ppm (Table 3), display a strong LREE/HREE fractionation with positive Ce and Sm anomalies and negative La, Pr, Eu anomalies (Fig. 6). The early Paleoproterozoic grain shows high LREE contents and flat REE pattern as compared to the younger grains.

4.2.3.2. SK-195-14-1. Zircon crystals in this sample are transparent, colourless to brownish with irregular to prismatic shape. Under CL, some grains show magmatic core rimmed by a bright overgrowth. Few grains display sector zoning and some are structureless. The grains vary in size from 30 to130 μm with aspect ratios of 2:1–1:1 (Fig. 5).

Sixteen spots were analysed from fifteen grains, among which one

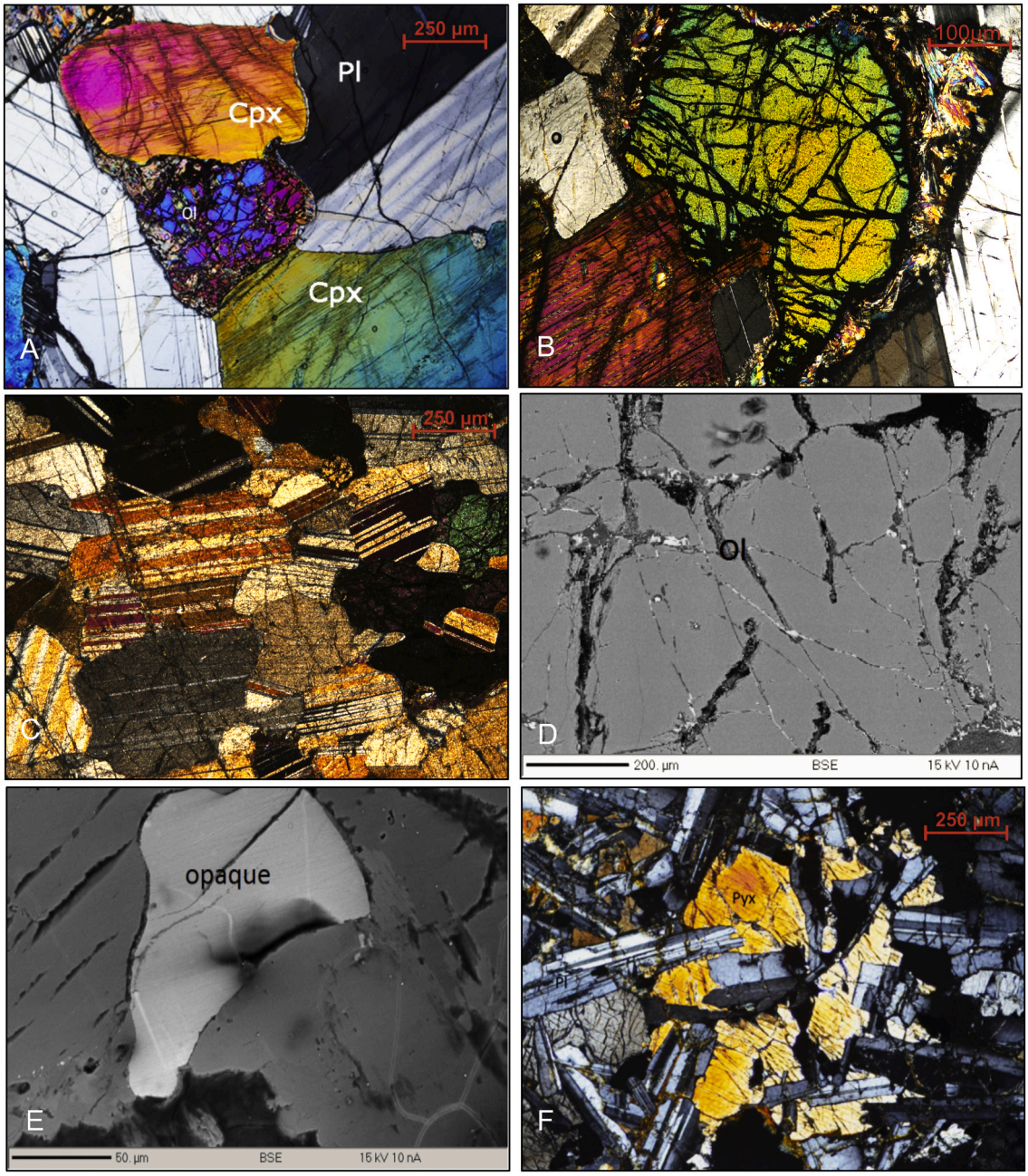

Fig. 2. Petrographic features of lower crustal gabbros from Central Indian Ridge (CIR). (A) Photomicrograph showing the mutual relationship of clinopyroxene, plagioclase and olivine grains in gabbros. Olivine occurs as intercumulus phase in the cumulate gabbro, (B) photomicrograph showing alteration along grain boundary of olivine grain, (C) photomicrograph showing typical cumulus layering in gabbro, (D) BSE image showing alteration along cross fractures of olivine grain, (E) BSE image showing the occurrence of opaque grain in gabbro, (F) photomicrograph showing the occurrence of ophitic and subophitic textures in microgbbro.

spot is excluded from age calculations due to low concordance. The remaining fifteen spots yield a wide range of age population, with $^{206}Pb/^{238}U$ ages ranging from Neoproterozoic to Cambrian (1142–449 Ma) (Table 2), and the youngest zircon showing $^{206}Pb/^{238}U$ age of 146 Ma (Fig. 7A). Their Th and U contents show a range of 464–2702 ppm and 765–4450 ppm respectively (Table 3), with Th/U ratios of 0.07–1.15. Most of the ratios are more than 0.1, suggesting magmatic origin.

Zircon grains from this sample show high total REE contents in the range of 1190–21,884 ppm (Table 3), higher than those in the previous sample. The REEs show a strong fractionation, positive Ce and Sm anomalies, negative La, Pr and Eu anomalies (Fig. 6). The older grains show higher LREE with flat REE patterns as compared to the younger grains.

4.2.3.3. SK-195-14-3. Zircon grains are very rare in this sample, and those obtained are mostly transparent and colourless or slightly brownish. The grains are small, euhedral to anhedral, and some are rounded. They range in length from 20 to 80 μm with aspect ratios of 1.5:1–1:1. In CL, pure bright recrystallized rims are also seen in some grains. A few grains show homogenous domains, and some show sector zoning (Fig. 5).

Eight grains were analysed and their ages show wide variation with the old grains yielding $^{207}Pb/^{206}Pb$ spot ages of 2525 Ma, 2395 Ma, 2039 Ma, 1925 Ma, and 1391 Ma, representing detrital zircons. The younger group of grains shows $^{206}Pb/^{238}U$ ages of 482, 407 Ma, 221 Ma,

Table 1
Major and trace element compositions of studied gabbros from Central Indian Ridge.

wt%	SK-195-9-1	SK-195-14-3	SK-195-14-4	SK-195-14-6	SK-195-14-7	SK-195-14-6	SK-195-14-7
SiO_2	48.55	46.11	43.38	44.72	43.58	41.05	43.79
TiO_2	0.14	0.32	0.27	1.45	0.71	0.32	0.48
Al_2O_3	15.39	16.87	14.81	14.20	12.44	16.96	15.98
$Fe_2O_3^{(T)}$	12.05	5.98	11.53	11.84	8.96	5.78	7.53
MnO	0.10	0.10	0.13	0.15	0.12	0.09	0.11
MgO	21.58	14.55	14.22	12.28	15.87	18.41	15.21
CaO	0.17	13.44	11.22	13.29	15.45	14.22	12.45
Na_2O	0.81	1.71	1.58	2.05	1.66	1.70	2.21
K_2O	0.05	0.08	0.13	0.15	0.09	0.08	0.13
P_2O_5	0.03	0.04	0.04	0.12	0.09	0.03	0.05
LOI	1.04	1.76	3.49	0.08	0.21	2.29	0.71
Total	99.91	100.96	100.80	100.33	99.18	100.93	98.65
Mg#	61	68	51	47	60	73	63
ppm							
Cr	1904	843	273	394	469	464	135
Co	86	40	60	54	21	35	36
Ni	399	51	73	53	33	48	33
Rb	0.9	0.9	1.6	1.9	0.9	0.6	1.1
Sr	6	110	119	112	64	107	146
Cs	0.04	0.03	0.04	0.04	0.04	0.02	0.04
Ba	9	12	19	22	9	10	15
Sc	7.80	34.19	12.35	38.83	35.07	36.63	43.03
V	35	126	61	177	72	137	171
Ta	1.20	0.07	0.22	0.38	0.63	0.25	0.11
Nb	0.74	1.24	1.33	7.62	2.69	0.69	0.79
Zr	7	11	18	42	13	9	18
Hf	0.14	0.26	0.42	1.02	0.33	0.22	0.42
Th	0.08	0.09	0.15	0.16	0.10	0.05	0.13
U	0.21	0.02	0.08	0.05	0.02	0.02	0.02
Y	0.93	8.22	11.38	53.81	20.54	7.75	15.05
La	0.23	0.60	1.54	2.56	1.35	0.29	0.81
Ce	0.40	1.80	4.26	8.38	3.93	0.87	2.38
Pr	0.05	0.24	0.62	1.57	0.72	0.15	0.46
Nd	0.27	1.37	3.24	9.75	4.15	0.99	3.82
Sm	0.06	0.57	1.03	4.03	1.57	0.48	1.05
Eu	0.03	0.36	0.54	1.35	0.46	0.33	0.60
Gd	0.05	0.56	0.84	3.78	1.44	0.51	1.04
Tb	0.02	0.25	0.34	1.63	0.62	0.23	0.45
Dy	0.09	1.08	1.46	7.24	2.64	1.02	2.01
Ho	0.02	0.26	0.36	1.74	0.62	0.25	0.48
Er	0.06	0.67	0.90	4.38	1.55	0.63	1.22
Tm	0.01	0.10	0.14	0.66	0.23	0.09	0.18
Yb	0.08	0.63	0.94	4.47	1.56	0.62	1.23
Lu	0.02	0.10	0.15	0.69	0.23	0.09	0.18
∑REE	1.39	8.60	16.37	52.23	21.08	6.55	15.90
Cu	8.86	28.05	15.84	31.19	15.81	24.92	25.72
Zn	117.58	100.26	214.01	261.09	57.88	33.58	57.19
Ga	0.73	10.73	14.42	15.43	6.77	9.92	13.26
Pb	1.87	1.46	2.00	2.09	1.93	1.30	2.16
$(La/Sm)_N$	2.47	0.68	0.96	0.41	0.56	0.39	0.50
$(Ce/Yb)_N$	1.43	0.79	1.25	0.52	0.70	0.39	0.54
$(Dy/Yb)_N$	0.73	1.14	1.03	1.08	1.13	1.10	1.10
$(Gd/Yb)_N$	0.54	0.74	0.74	0.70	0.76	0.68	0.70
Eu/Eu*	1.41	1.94	1.73	1.04	0.93	2.04	1.73
Ce/Ce*	0.86	1.17	1.07	1.00	0.97	1.00	0.94
Dy/Dy*	0.58	1.28	0.98	1.42	1.31	1.54	1.38
Hf/Hf*	2.95	0.69	0.57	0.39	0.32	0.71	0.55
Zr/Y	8.04	1.34	1.54	0.79	0.63	1.16	1.20
Nb/Y	0.80	0.15	0.12	0.14	0.13	0.09	0.05
Zr/Sm	122.32	19.28	16.96	10.50	8.26	18.72	17.08
Nb/Zr	0.10	0.11	0.08	0.18	0.21	0.08	0.04
Nb/La	3.18	2.05	0.87	2.97	1.99	2.37	0.98
Zr/Nb	10.05	8.87	13.16	5.55	4.81	12.96	22.74
Nb/Yb	9.45	1.96	1.41	1.70	1.72	1.12	0.65
Nb/Th	9.28	13.38	9.12	48.10	27.05	14.01	5.89
Zr/Hf	54.30	42.44	42.11	41.29	38.69	41.43	42.68
Th/Ce	0.20	0.05	0.03	0.02	0.03	0.06	0.06
Yb/Sm	1.29	1.11	0.91	1.11	0.99	1.29	1.16
Sr/Y	6.86	13.35	10.43	2.08	3.14	13.81	9.73
Yb/La	0.34	1.05	0.61	1.74	1.15	2.12	1.51
Gd/Yb	0.65	0.89	0.89	0.84	0.92	0.83	0.85
Th/Nb	0.11	0.07	0.11	0.02	0.04	0.07	0.17
Ba/Nb	11.95	9.62	13.96	2.88	3.29	14.08	18.41
Ba/Th	110.94	128.76	127.30	138.70	88.91	197.30	108.38

(*continued on next page*)

Table 1 (*continued*)

wt%	SK-195-9-1	SK-195-14-3	SK-195-14-4	SK-195-14-6	SK-195-14-7	SK-195-14-6	SK-195-14-7
Rb/Nb	1.17	0.70	1.21	0.25	0.35	0.92	1.43
Ba/La	38.01	19.76	12.08	8.57	6.54	33.39	17.98
Pb/Ce	4.65	0.81	0.47	0.25	0.49	1.50	0.91
Zr/Hf	54.30	42.44	42.11	41.29	38.69	41.43	42.68
Nb/Ta	0.62	16.87	6.07	19.92	4.29	2.80	6.89

wt%	SK-195-14-8	SK-195-14-9	SK-195-14-10	SK-195-14-11	SK-195-14-12
SiO_2	41.72	43.82	42.11	43.75	43.72
TiO_2	0.29	0.58	0.36	0.48	0.58
Al_2O_3	16.97	15.01	16.10	15.97	15.84
$Fe_2O_3^{(T)}$	5.71	7.65	7.68	7.55	7.62
MnO	0.08	0.11	0.10	0.11	0.11
MgO	16.92	15.21	16.32	14.94	15.28
CaO	15.69	15.45	15.10	13.75	13.47
Na_2O	1.75	2.38	1.98	2.21	2.39
K_2O	0.07	0.10	0.12	0.13	0.10
P_2O_5	0.03	0.04	0.04	0.05	0.04
LOI	1.29	0.22	0.12	0.74	0.66
Total	100.52	100.57	100.03	99.68	99.81
Mg#	72	63	65	63	63
ppm					
Cr	608	58	195	125	60
Co	36	31	43	36	33
Ni	55	25	49	32	35
Rb	0.7	0.9	1.1	1.2	0.9
Sr	116	130	106	141	133
Cs	0.02	0.03	0.05	0.04	0.03
Ba	11	20	10	17	15
Sc	32.55	48.53	36.21	41.37	50.09
V	118	219	132	164	222
Ta	0.27	0.13	0.18	0.85	0.86
Nb	0.33	0.58	0.44	1.07	0.72
Zr	8	20	13	18	20
Hf	0.19	0.49	0.31	0.44	0.49
Th	0.08	0.08	0.06	0.16	0.14
U	0.02	0.03	0.02	0.04	0.03
Y	6.58	20.24	10.46	14.75	21.16
La	0.43	0.77	0.58	0.80	0.77
Ce	1.00	2.31	1.66	2.31	2.30
Pr	0.16	0.45	0.29	0.42	0.45
Nd	1.01	2.83	1.71	2.49	2.89
Sm	0.43	1.26	0.72	1.07	1.31
Eu	0.31	0.66	0.41	0.60	0.67
Gd	0.44	1.30	0.70	1.04	1.36
Tb	0.21	0.58	0.31	0.45	0.61
Dy	0.89	2.66	1.37	1.98	2.84
Ho	0.22	0.65	0.34	0.48	0.68
Er	0.53	1.65	0.85	1.20	1.74
Tm	0.08	0.25	0.13	0.18	0.26
Yb	0.53	1.67	0.85	1.17	1.76
Lu	0.08	0.26	0.13	0.19	0.27
∑REE	6.31	17.30	10.05	14.37	17.91
Cu	29.71	13.36	16.02	19.71	14.12
Zn	37.65	81.94	49.22	70.86	64.54
Ga	10.84	14.36	10.94	13.26	15.61
Pb	1.23	1.92	1.59	2.11	1.63
$(La/Sm)_N$	0.64	0.39	0.52	0.48	0.38
$(Ce/Yb)_N$	0.52	0.38	0.54	0.55	0.36
$(Dy/Yb)_N$	1.12	1.07	1.08	1.13	1.08
$(Gd/Yb)_N$	0.68	0.64	0.68	0.73	0.64
Eu/Eu*	2.13	1.56	1.76	1.71	1.52
Ce/Ce*	0.92	0.94	0.99	0.97	0.95
Dy/Dy*	1.32	1.50	1.35	1.41	1.54
Hf/Hf*	0.66	0.60	0.66	0.63	0.58
Zr/Y	1.19	0.96	1.26	1.22	0.94
Nb/Y	0.05	0.03	0.04	0.07	0.03
Zr/Sm	18.03	15.49	18.30	16.72	15.20
Nb/Zr	0.04	0.03	0.03	0.06	0.04
Nb/La	0.77	0.76	0.76	1.34	0.94
Zr/Nb	23.49	33.58	29.95	16.84	27.75
Nb/Yb	0.63	0.35	0.52	0.91	0.41
Nb/Th	4.32	7.16	6.91	6.78	4.98
Zr/Hf	42.14	40.19	42.08	40.98	40.73
Th/Ce	0.08	0.04	0.04	0.07	0.06

(*continued on next page*)

Table 1 (*continued*)

wt%	SK-195-14-8	SK-195-14-9	SK-195-14-10	SK-195-14-11	SK-195-14-12
Yb/Sm	1.22	1.32	1.18	1.09	1.34
Sr/Y	17.56	6.40	10.17	9.59	6.30
Yb/La	1.22	2.17	1.47	1.47	2.30
Gd/Yb	0.82	0.78	0.82	0.89	0.77
Th/Nb	0.23	0.14	0.14	0.15	0.20
Ba/Nb	31.51	35.11	23.08	16.15	20.55
Ba/Th	136.11	251.46	159.51	109.48	102.32
Rb/Nb	2.10	1.60	2.44	1.11	1.30
Ba/La	24.26	26.55	17.61	21.64	19.27
Pb/Ce	1.24	0.83	0.96	0.91	0.71
Zr/Hf	42.14	40.19	42.08	40.98	40.73
Nb/Ta	1.26	4.63	2.44	1.26	0.84

Nomalization factors after Sun and McDonough (1989).

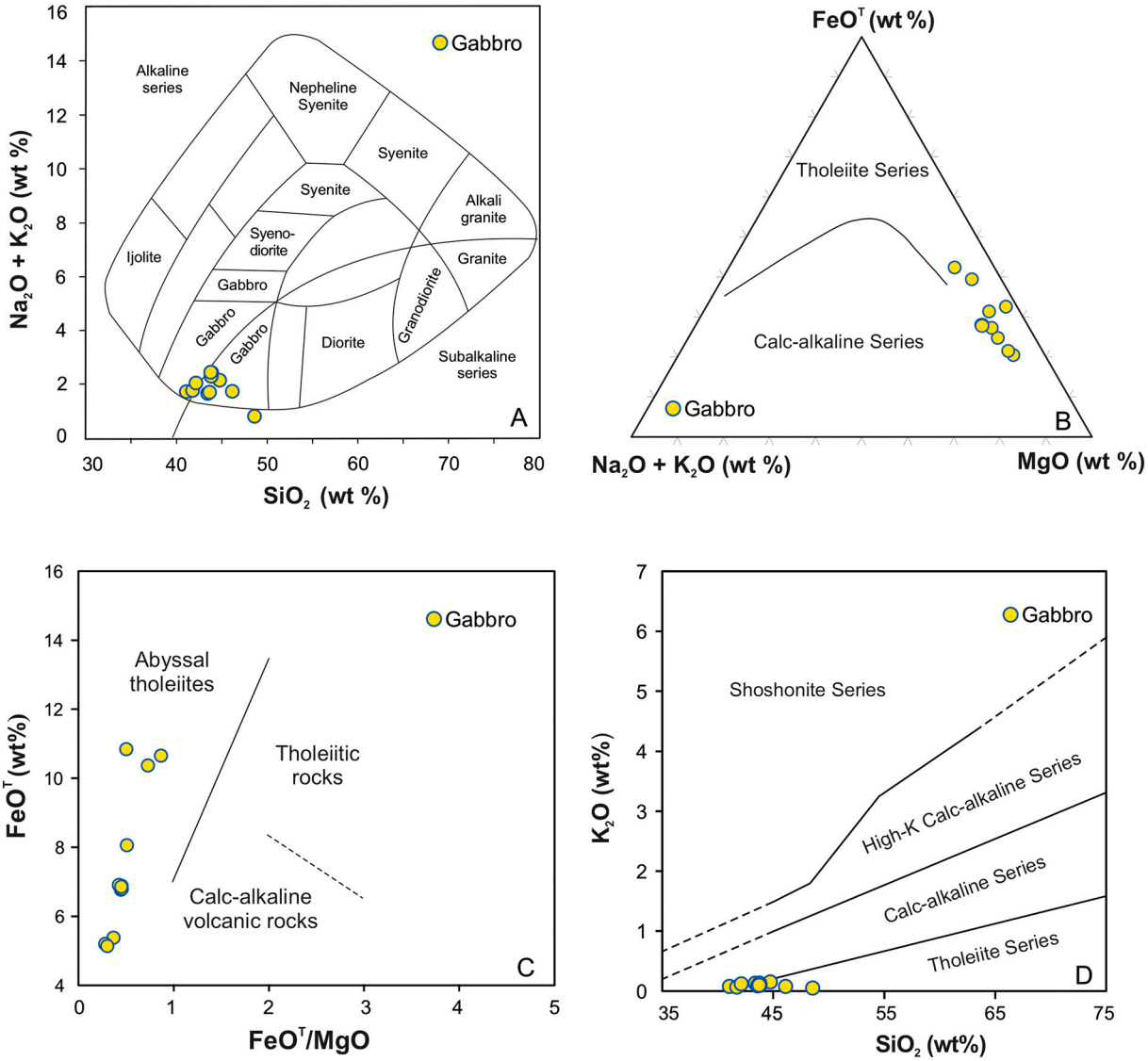

Fig. 3. (A) Plots of the studied gabbros in total alkali-silica (TAS) diagram (after Cox et al., 1979) adapted by Wilson (1989) for plutonic igneous rocks. The curved solid line (after Irvine and Baragar, 1971) subdivides the alkaline from subalkaline rocks, (B) Central Indian Ridge gabbros showing a tholeiitic nature in (Na_2O + K_2O) – FeOT- MgO (AFM) diagram (after Irvine and Baragar, 1971), (C) plots of studied gabbros in FeO^T/MgO vs. FeO^T diagram indicating their abyssal tholeiitic nature (D) plots of studied gabbros reflecting low K tholeiitic trend in SiO_2 vs. K_2O diagram.

127 Ma (Fig. 7B) (Table 2). Their Th and U contents are 19.5–462 ppm and 15.7–1007 ppm (Table 2) respectively, with Th/U ratios of 0.37–1.24.

Zircon REE contents in this sample show a wide range of 175–1739 ppm (Table 3), with prominent LREE/HREE fractionation, positive Ce and Sm anomalies, as well as negative La, Pr, Nd and Eu anomalies (Fig. 6). The older zircon grains show more flat REE with LREE enrichment.

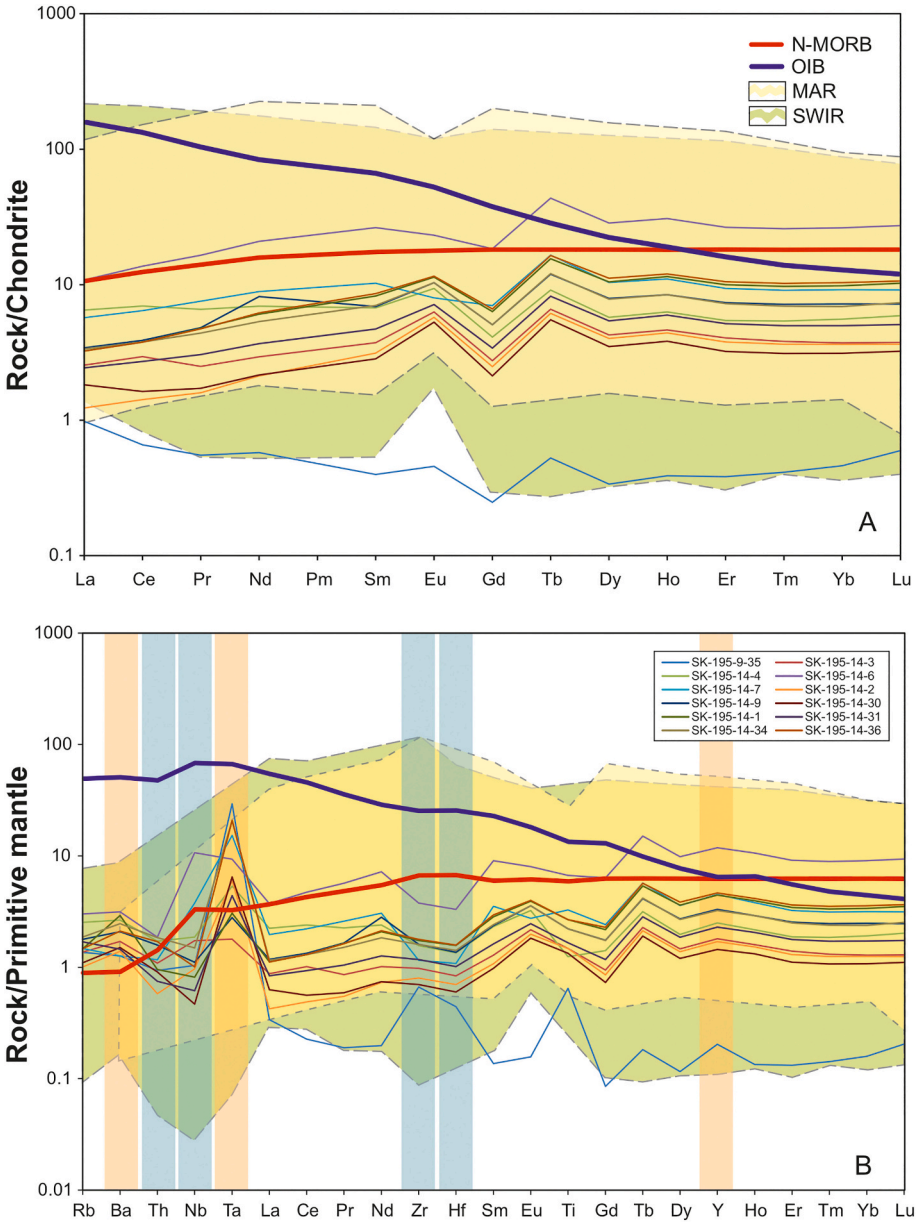

Fig. 4. (A) Chondrite normalized REE and (B) primitive mantle normalized multi-element spider diagrams for the studied gabbros. Normalization values are from Sun and McDonough, 1989. Chondrite and primitive mantle normalized REE and trace element abundances of CIR gabbros are compared with that of N-MORB, OIB, MAR and SWIR [data source: MAR gabbro data are from (Agar et al., 1997; Bonatti et al., 1971; Casey, 1997; Cortesogno et al., 2000; Fletcher et al., 1997; Hekinian et al., 2000) and SWIR gabbro data are from (Bach et al., 2001; Casey et al., 2007; Kumagai et al., 2003; Yi et al., 2014).

4.2.3.4. SK-195-14-2. Zircon grains from this sample can be divided into two groups. One group is very small and transparent with euhedral to subhedral crystal morphology and generally dark under CL, suggesting magmatic grains with high U contents. The second group is dark brownish and bright in CL. They show angular morphology, and some are elongated or triangular. The zircon grains show wide range of length from 30 to 300 μm with aspect ratios of 3.5:1–1:1 (Fig. 5). The grains display sector zoning or banded zoning, and some grains are structureless. A few grains show weak core-rim texture.

A total of forty two spots were analysed from thirty six grains. Excluding twenty two spots due to low concordance and unreliable signal, the remaining twenty spots can be divided into two groups. One group includes two spots with $^{206}Pb/^{238}U$ ages of 792 Ma and 775 Ma, and possessing Th contents of 364 ppm and 134 ppm, U contents of 1151 ppm and 983 ppm (Table 2), and Th/U ratios in the range of 0.32 and 0.14. Another group contains eighteen spots which yield Pleistocene weighted mean $^{206}Pb/^{238}U$ ages of 1.296 ± 0.01 Ma (MSWD = 0.94) (Fig. 7C). These grains have high Th and U contents of 1336–14,574 ppm and 1333–7025 ppm respectively and very high Th/U ratios (0.76–4.42). Their total Pb contents are very low (1.2–17.5 ppm), and hence low ^{207}Pb content resulting in low concordance. Although their concordance are low, when plotted on the concordia diagram, all the spots fall along the concordia line.

Zircon REE data from this sample can also be divided into two groups based on their ages. Grains with Neoproterozoic age possess REE contents of 6251 ppm and 4453 ppm. One grain shows slightly flat REE pattern, and another grain is strongly depleted in LREE but still higher than the younger group. Both grains display negative Eu anomalies. The high REE associated with high Th, U contents suggest magmatic crystallization of these grains. Most of the grains show positive Ce and Sm anomalies and negative La, Pr, Nd and Eu anomalies (Fig. 6).

In summary, zircon grains in samples SK-195-9-6, SK-195-14-1, SK-195-14-3 show a wide range of ages ($^{207}Pb/^{206}Pb$ age of: 2525–1391 Ma, $^{206}Pb/^{238}U$ age of: 1142–221 Ma, 173–127 Ma). All the grains are concordant with no major Pb loss. Zircon grains in sample SK-195-14-1 however belong to two distinct groups: Neoproterozoic with $^{206}Pb/^{238}U$ age of 792 Ma and 775 Ma, and Pleistocene with a weighted mean $^{206}Pb/^{238}U$ age of 1.296 ± 0.01 Ma (MSWD = 0.94). A compilation of

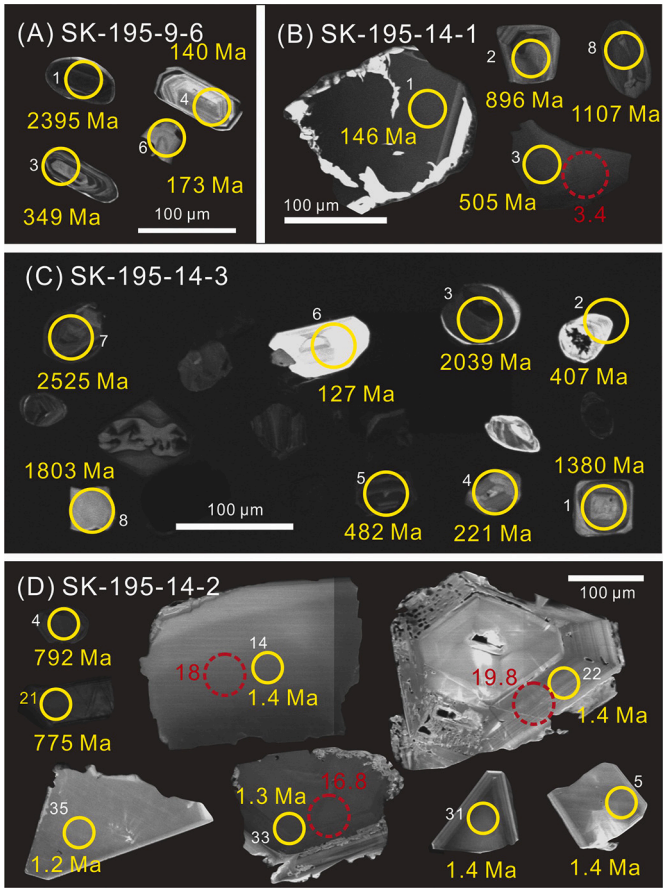

Fig. 5. Representative cathodoluminescence (CL) images of the analysed zircon grains from the CIR gabbros. Yellow circles represent U—Pb ages and red circles represent $\varepsilon_{Hf}(t)$ values. The U—Pb zircon data having at least 93% concordance have been used for interpretation in this study (Table 3). (For interpretation of the references to colour in this figure legend, the reader is referred to the web version of this article.)

zircon U—Pb age data from all the samples indicate a wide spectrum consistent with multiple thermo-tectonic events (Fig. 8).

Due to the scarcity of zircon grains and their relatively small size, only limited large grains were anlaysed for Lu—Hf, either on the same domains or on adjacent domains from where the U—Pb age data were gathered. In sample SK-195-14-1 only one grain was analysed which shows initial $^{176}Hf/^{177}Hf$ value of 0.28258189. The $\varepsilon_{Hf}(t)$ shows positive value of 3.4, suggesting the juvenile mantle source for the parent magma.

Four grains were analysed from sample SK-195-14-2, and their initial $^{176}Hf/^{177}Hf$ values show a range of 0.283232–0.283279. The $\varepsilon_{Hf}(t)$ are positive with high values of 16.8–19.8, suggesting the parent magma was derived from juvenile mantle components (Table S1).

5. Discussion

5.1. Petrogenetic implications and mantle heterogeneity

The trace and REE abundances of the CIR gabbros (Fig. 4), normalized with respect to primitive mantle and chondrite values respectively, depict a consistent coherence with that of MAR and SWIR and characteristically reflect depleted compositions of the parent magmas in comparison with the trace and REE compositions of average OIB (Gale et al., 2013; Saunders et al., 1988; Sun and McDonough, 1989). However, the chondrite-normalized LREE patterns for the studied samples depict an enriched trend in comparison with typically flat LREE patterns observed for depleted N-MORB. In conjunction with this, elevated LILE, LREE, HFSE abundances and lack of positive Nb, Zr and Hf anomalies narrow down the possibility of mantle plume influence or contribution from plume-derived melts with OIB component. Positive primitive mantle normalized Nb anomalies in conjunction with pronounced LREE/HREE fractionation are observed in the following scenarios.

(i) OIB magmas in intraplate tectonic settings derived from deep mantle plumes carrying a HIMU component. This HIMU signature can be equated with recycled subduction component in ancient oceanic slab subducted to the lower mantle and eventually entrained by ascending mantle plumes or upwelling asthenospheric mantle.
(ii) Adakites, Nb-enriched basalts (NEB) and high Nb basalts (HNB) generated by shallow, flat subduction of hot, young oceanic lithosphere and hybridization of peridotitic sub-arc mantle wedge by eclogitic slab melts retaining fluid immobile HSFE during matured stage of subduction.
(iii) Melts incorporating Nb bearing phases like amphibole in hydrated mantle wedge in a subduction regime.

Thus, enhanced Nb concentrations with LREE enrichment over HREE provide compelling evidence for: (a) entrapment of HIMU component carrying recycled ancient subducted oceanic slab by ascending mantle plume/upwelling asthenosphere, (b) slab melting and mantle wedge hybridization at matured stage of subduction, or (c) subducted slab tearing, break-off and passage of asthenospheric mantle carrying OIB-type component at termination of subduction. In this study, LILE>HFSE, LREE> HFSE and depleted primitive-mantle normalized Nb, Th, Zr—Hf patterns for these CIR gabbros preclude the role of mantle plume component or subducted slab and reconciles delamination, convective downwelling and recycling of ancient subduction-modified, metasomatized continental lithosphere into the asthenosphere thereby accounting for the enriched signatures of magmas precursor to these rocks. HFSE and REE variations reflected on Nb/La vs. $(La/Sm)_N$ plot (Fig. 9A) conform to the origin and emplacement of the studied gabbros in an oceanic environment. Th-Nb-Ce compositions for oceanic basalts and their derivatives constrain their mantle source characteristics in terms of mixing between three mantle components viz. DMM (Depleted MORB mantle), RSC (recycled residual slab component) and SDC (recycled subduction-derived component) (Safonova et al., 2008; Saha et al., 2020; Saunders et al., 1988). The enriched composition of sub-oceanic upper mantle beneath a mid-oceanic ridge-rift system can be equated with (i) influence of a mantle plume carrying recycled residual slab component (RSC) from paleosubduction events causing low Ce/Nb and Th/Nb and (ii) infiltration of recycled subduction–derived components (SDC) through lithosphere-asthenosphere interaction manifested in terms of high Th/Nb and Ce/Nb. Recycling of continental lithosphere by (a) subduction-driven delamination and convective downwelling during collisional orogeny and continental amalgamation processes or (b) thermal erosion, convection removal and recycling of crust in response to continental disintegration and opening of ocean basins also account for the geochemical diversity of the upper mantle (Ashwal et al., 2017; Barruol et al., 2019; Levander et al., 2014; Scott et al., 2014, 2019; Zhang et al., 2018). The geochemical attributes of the lower oceanic crust gabbros from CIR marked by relatively high Ce/Nb but low Th/Nb reflect a deviation from typical, depleted N-MORB (DMM) pattern and shows affinity to *E*-MORB. This E-MORB signature for the CIR gabbros is attributed to enriched lithospheric input into the depleted asthenospheric mantle. Their HFSE and REE compositions (Th/Ta-Th/Hf-Th/Yb and Zr/Ta* vs. Ce/Y) (Fig. 9B and C) depict a marked deviation from typical depleted N-MORB compositions and the sample array conforms to an E-MORB affinity. The studied CIR gabbros straddle fields of N-MORB and E-MORB on Nb/La vs. Ba/Rb (Fig. 9D) plot thereby complying with a transitional and heterogeneous chemistry of the source mantle. The Nb/La vs. La/Yb variation plots (Fig. 9E) suggest a

Table 2
LA-ICP-MS zircon age data from studied gabbro samples.

Sample spot	Element concentration (ppm)			Th/U	Isotope ratios (±1σ)					
	Pb	Th	U		$^{207}Pb/^{206}Pb$		$^{207}Pb/^{235}U$		$^{206}Pb/^{238}U$	
SK-195-9-6-01	217.1	100.4	211.2	0.48	0.1544	0.0078	9.373	0.4958	0.4383	0.01
SK-195-9-6-03	64.8	320.4	290.7	1.1	0.0559	0.0054	0.4277	0.0379	0.0556	0.0016
SK-195-9-6-04	20.6	232.6	333	0.7	0.0491	0.0055	0.1468	0.0159	0.0219	0.0006
SK-195-14-1-01	88.1	898.9	1776.7	0.51	0.049	0.0051	0.1544	0.0154	0.0228	0.0006
SK-195-14-1-02	404.6	615.8	1282.2	0.48	0.0696	0.0034	1.4687	0.0704	0.1521	0.0024
SK-195-14-1-03	153.5	463.7	884.2	0.52	0.0565	0.0049	0.5757	0.0504	0.0736	0.0017
SK-195-14-1-04	534.8	1727.7	2223.4	0.78	0.0574	0.0039	0.6294	0.0421	0.079	0.0016
SK-195-14-1-05	294.1	939.9	1706.7	0.55	0.0561	0.0043	0.5607	0.0423	0.0721	0.0019
SK-195-14-1-06	925.5	1403.6	1222.1	1.15	0.0774	0.0043	2.0408	0.1139	0.1902	0.0042
SK-195-14-1-07	688.8	881.2	1245.9	0.71	0.0793	0.0043	2.1353	0.1167	0.1938	0.0036
SK-195-14-1-08	600	874.7	1052.5	0.83	0.0785	0.0039	1.9093	0.1004	0.1752	0.0032
SK-195-14-1-09	596.3	1964.6	1876.4	1.05	0.0616	0.0038	0.8837	0.0534	0.1062	0.0054
SK-195-14-1-11	349.3	328.1	4449.9	0.07	0.0578	0.003	0.6508	0.0324	0.0813	0.0013
SK-195-14-1-12	480.2	1468.7	1779	0.83	0.0584	0.0046	0.6718	0.0514	0.0833	0.002
SK-195-14-1-13	1164.2	2702.3	2725.7	0.99	0.0704	0.0035	1.192	0.059	0.1225	0.0023
SK-195-14-1-14	332.5	547.2	765.3	0.72	0.0752	0.0044	1.7386	0.0995	0.1676	0.0034
SK-195-14-1-15	442	797.3	1510.8	0.53	0.065	0.0031	1.1435	0.0539	0.1274	0.0022
SK-195-14-1-16	336.4	548.4	1469.2	0.37	0.0652	0.003	1.1606	0.0585	0.1284	0.0022
SK-195-14-3-01	190.8	163.1	444.6	0.37	0.0884	0.0046	2.9381	0.1532	0.2387	0.0045
SK-195-14-3-02	21.6	62.8	153.2	0.41	0.0578	0.0092	0.5215	0.0778	0.0652	0.0028
SK-195-14-3-03	88.3	45.8	142.6	0.32	0.1256	0.0088	6.2853	0.4214	0.3615	0.0107
SK-195-14-3-04	29.4	208.3	272.9	0.76	0.053	0.0074	0.2515	0.033	0.0348	0.0013
SK-195-14-3-05	84.8	255.7	426.2	0.6	0.0569	0.005	0.6106	0.0538	0.0776	0.0019
SK-195-14-3-06	43	462.5	1007.4	0.46	0.0486	0.0049	0.1344	0.0134	0.02	0.0006
SK-195-14-3-07	166.6	79.4	141.4	0.56	0.1667	0.0089	11.2776	0.6053	0.488	0.0105
SK-195-14-3-08	23.1	19.5	15.7	1.24	0.1179	0.0162	5.094	0.6276	0.3227	0.0153
SK-195-14-2-24	11.5	14,574.3	4912.4	2.97	0.05646	0.039325	0.001274	0.000666	0.000201	0.000024
SK-195-14-2-04	260.5	364	1150.9	0.32	0.064431	0.004113	1.166784	0.072975	0.130676	0.002396
SK-195-14-2-21	149.2	133.6	982.8	0.14	0.065637	0.004768	1.16812	0.082062	0.1277	0.002451

Sample spot	Age (Ma ± 1σ)						Concordance	Con vs.Dis
	$^{207}Pb/^{206}Pb$		$^{207}Pb/^{235}U$		$^{206}Pb/^{238}U$			
SK-195-9-6-01	2395	85	2375	49	2343	45	98%	Concordant
SK-195-9-6-03	450	215	362	27	349	10	96%	Concordant
SK-195-9-6-04	154	263	139	14	140	4	99%	Concordant
SK-195-14-1-01	146	248	146	14	146	4	99%	Concordant
SK-195-14-1-02	917	100	918	29	912	14	99%	Concordant
SK-195-14-1-03	472	193	462	33	458	10	99%	Concordant
SK-195-14-1-04	506	157	496	26	490	9	98%	Concordant
SK-195-14-1-05	457	170	452	28	449	12	99%	Concordant
SK-195-14-1-06	1131	111	1129	38	1123	23	99%	Concordant
SK-195-14-1-07	1189	107	1160	38	1142	19	98%	Concordant
SK-195-14-1-08	1158	100	1084	35	1041	18	95%	Concordant
SK-195-14-1-09	659	133	643	29	651	31	98%	Concordant
SK-195-14-1-11	524	124	509	20	504	8	98%	Concordant
SK-195-14-1-12	546	170	522	31	516	12	98%	Concordant
SK-195-14-1-13	939	102	797	27	745	13	93%	Concordant
SK-195-14-1-14	1073	119	1023	37	999	19	97%	Concordant
SK-195-14-1-15	776	109	774	26	773	13	99%	Concordant
SK-195-14-1-16	789	96	782	28	779	13	99%	Concordant
SK-195-14-3-01	1391	101	1392	40	1380	24	99%	Concordant
SK-195-14-3-02	524	348	426	52	407	17	95%	Concordant
SK-195-14-3-03	2039	125	2016	59	1989	51	98%	Concordant
SK-195-14-3-04	332	322	228	27	221	8	96%	Concordant
SK-195-14-3-05	487	196	484	34	482	11	99%	Concordant
SK-195-14-3-06	132	250	128	12	127	4	99%	Concordant
SK-195-14-3-07	2525	90	2546	50	2562	46	99%	Concordant
SK-195-14-3-08	1925	248	1835	105	1803	75	98%	Concordant
SK-195-14-2-24	477.8	1240.7	1.3	0.7	1.3	0.2	99%	Concordant
SK-195-14-2-04	767	135	785	34	792	14	99%	Concordant
SK-195-14-2-21	794	161	786	38	775	14	98%	Concordant

lithosphere-asthenosphere interaction for the origin of the studied rocks. The accretion of lower oceanic crust gabbros beneath the CIR can be translated in terms of melt extraction by shallow level melting of a chemically heterogeneous upper mantle characterized by depleted asthenosphere and recycled subducted lithospheric components. On Th/Yb vs. Nb/Yb plot (Fig. 9F), the sample array reflects a transitional composition from N-MORB to E-MORB; the samples falling out of the MORB-OIB domain distinctly conform to contributions from subduction-derived components in the source mantle. A distinct magmatic enrichment trend is reflected from the sample plots on U/Nb vs. Nb/Zr diagram (Fig. 10A). The array of sample plots on Nb/Zr vs. Th/Zr diagram (Fig. 10B) in conjunction with Nb/Th $>$ 1 attests to melt related enrichment of source attributed to mixing of depleted asthenosphere and enriched recycled lithospheric components. A transitional depleted to enriched mantle signature concomitant to recycling of subducted lithospheric components into asthenospheric mantle is corroborated by

Table 3
LA-ICP-MS zircon trace element data from studied gabbros.

Sample spot	Element (ppm)									
	U	La	Ce	Pr	Nd	Sm	Eu	Gd	Tb	Dy
SK-195-9-6-01	211	3.36	46.84	2.75	15.31	5.02	2.21	16.62	4.26	54.51
SK-195-9-6-03	291	0.02	34.43	0.08	1.66	3.43	0.63	16.8	4.96	69.59
SK-195-9-6-04	333	0.09	15.73	0.1	0.98	2.17	0.45	17.45	6.29	96.88
SK-195-14-1-01	1777	–	25.41	0.02	1.05	2.23	1.42	22.47	8.18	133.83
SK-195-14-1-02	1282	2.65	54.67	1.09	10.93	20.64	0.42	141.02	53.59	789.81
SK-195-14-1-03	884	1.55	41.72	1.28	15.46	6.19	2.92	27.78	9.56	117.89
SK-195-14-1-04	2223	0.14	118.63	0.79	6.81	16.34	4.61	104.86	35.37	503.89
SK-195-14-1-05	1707	0.75	38.37	0.55	8.88	11.1	2	82.46	29.32	404.68
SK-195-14-1-06	1222	0.35	49.56	1.41	23.67	36.51	1.71	170.23	52.28	647.12
SK-195-14-1-07	1246	0.02	38.64	0.11	3.48	7.08	0.36	46.13	15.79	199.03
SK-195-14-1-08	1053	3.09	47.27	1.02	8.94	10.3	1.44	50.51	15.49	181.99
SK-195-14-1-09	1876	23.36	160.78	9.04	46.65	25.1	5	96.74	34.38	447.97
SK-195-14-1-11	4450	1.77	14.89	1.23	6.53	2.08	3.1	10.52	3.9	74.32
SK-195-14-1-12	1779	41.18	183.39	10.34	41.42	31.32	3.06	117.9	42.58	542.5
SK-195-14-1-13	2726	81.89	482.8	41.03	281.25	258.1	8.3	1161.79	345.19	4114.72
SK-195-14-1-14	765	0.4	63.09	0.94	10.32	21.49	2.67	88.83	33.67	442.28
SK-195-14-1-15	1511	0.11	49.54	0.13	3.56	9.09	0.72	56.29	18.07	256.5
SK-195-14-1-16	1469	0.04	36.02	0.1	1.43	4.4	0.59	26.27	9.62	135.37
SK-195-14-3-01	445	1.74	9.83	0.77	4.76	4.8	0.04	23.9	8.64	138.85
SK-195-14-3-02	153	–	8.26	0.1	0.47	1.47	0.21	12.65	5.2	78.41
SK-195-14-3-03	143	7.7	57.17	1.45	6.59	2.53	1.17	6.25	1.98	27.47
SK-195-14-3-04	273	0.15	4.85	0.16	2.42	4.4	0.59	24.59	6.84	87.69
SK-195-14-3-05	426	0.05	13.56	0.18	4.42	7.64	1.61	42.5	13.55	175.75
SK-195-14-3-06	1007	0.09	22.47	0.06	1.82	3.37	0.78	26.6	11.5	179.76
SK-195-14-3-07	141	0.25	11.93	0.26	1.32	3.69	1.48	18.22	5.46	66.22
SK-195-14-3-08	16	–	6.19	–	0.12	0.26	0.1	2.13	0.8	13.41
SK-195-14-2-24	4912	0.05	235.06	1.92	31.32	78.41	2.79	507.56	190.42	2677.8
SK-195-14-2-04	1151	139.08	351.15	44.03	207.11	54.51	1.07	113.18	42.28	593.69
SK-195-14-2-21	983	–	1.53	0.13	1.19	6.81	0.14	77.33	33.88	524.43

Sample spot	Element (ppm)				
	Ho	Er	Tm	Yb	Lu
SK-195-9-6-01	19.83	93.68	20.96	236.99	46.96
SK-195-9-6-03	25.35	129.75	30.17	349.69	64.31
SK-195-9-6-04	38.4	204.12	45.98	524.45	100.85
SK-195-14-1-01	57.12	307.18	78.34	978.52	204.82
SK-195-14-1-02	293.14	1375.05	268.83	2575.41	407.19
SK-195-14-1-03	44.48	221.2	48.71	547.8	103.32
SK-195-14-1-04	185.32	914.62	189.76	2037.95	369.69
SK-195-14-1-05	151.58	733.83	151.6	1575.05	284.83
SK-195-14-1-06	210.06	943.97	172.61	1701.98	274.57
SK-195-14-1-07	79.84	379.43	74.54	778.17	133.71
SK-195-14-1-08	61.9	271.5	54.29	547.97	93.37
SK-195-14-1-09	164.33	817.12	170.78	1849.37	342.09
SK-195-14-1-11	31.41	191.32	53.27	686.12	150.68
SK-195-14-1-12	190.82	885.26	174.42	1797.09	306.47
SK-195-14-1-13	1304.26	5156.25	849.25	6856.07	943.18
SK-195-14-1-14	160.97	769.61	155.92	1609.6	273.71
SK-195-14-1-15	90.32	430.32	88.97	909.08	156.79
SK-195-14-1-16	51.56	258.63	54.52	609.96	110.43
SK-195-14-3-01	50.84	251.72	51.1	533.1	91.03
SK-195-14-3-02	35.13	194.69	46.23	551.89	112.07
SK-195-14-3-03	9.87	54.48	12.25	150.71	29.26
SK-195-14-3-04	30.63	151.89	32.79	331.53	58.52
SK-195-14-3-05	61.51	291.35	57.45	606.89	103.97
SK-195-14-3-06	72.46	362.57	77.61	828.91	151.02
SK-195-14-3-07	22.21	105.43	20.82	235.57	41.93
SK-195-14-3-08	5.32	28.85	7.21	90.96	19.23
SK-195-14-2-24	1018.23	5012.45	1003.97	9838.26	1506.97
SK-195-14-2-04	228.16	1159.78	240.67	2623.37	453.08
SK-195-14-2-21	191.15	937.96	201.97	2118.6	357.74

Zr/Nb vs. Nb/Th plot (Fig. 10C). A chemically heterogeneous source mantle with input from recycled subduction-derived components accounts for the sample plots straddling the N-MORB and arc fields of Th_N vs. Nb_N diagram (Fig. 10D).

The CIR gabbros having Dy/Yb ratios (<1) indicate parent melt extraction from a spinel peridotite mantle at shallow level. The studied samples have variable 0.3–7.62 Nb (ppm) and lower Zr (7–42 ppm) contents compared to the N-MORB (Nb: 2.33 ppm, Zr: 74 ppm) implying their generation from a depleted to enriched mantle source (Sun and McDonough, 1989). The higher Zr/Hf (avg. 42.42) and Zr/Sm (avg. 24.74) in conjunction with lower Nb/Ta (avg. 5.66) values for these CIR gabbros in comparison with that of primitive mantle (Zr/Hf: 36, Zr/Sm: 25 and Nb/Ta: 17) corroborate infiltration of metasomatized lithospheric components into asthenospheric mantle thereby imparting *E*-MORB like incompatible trace element enrichment. The Zr/Nb ratios of these rocks depict a wide range from 4.81–33.58 (avg. 17.48) in

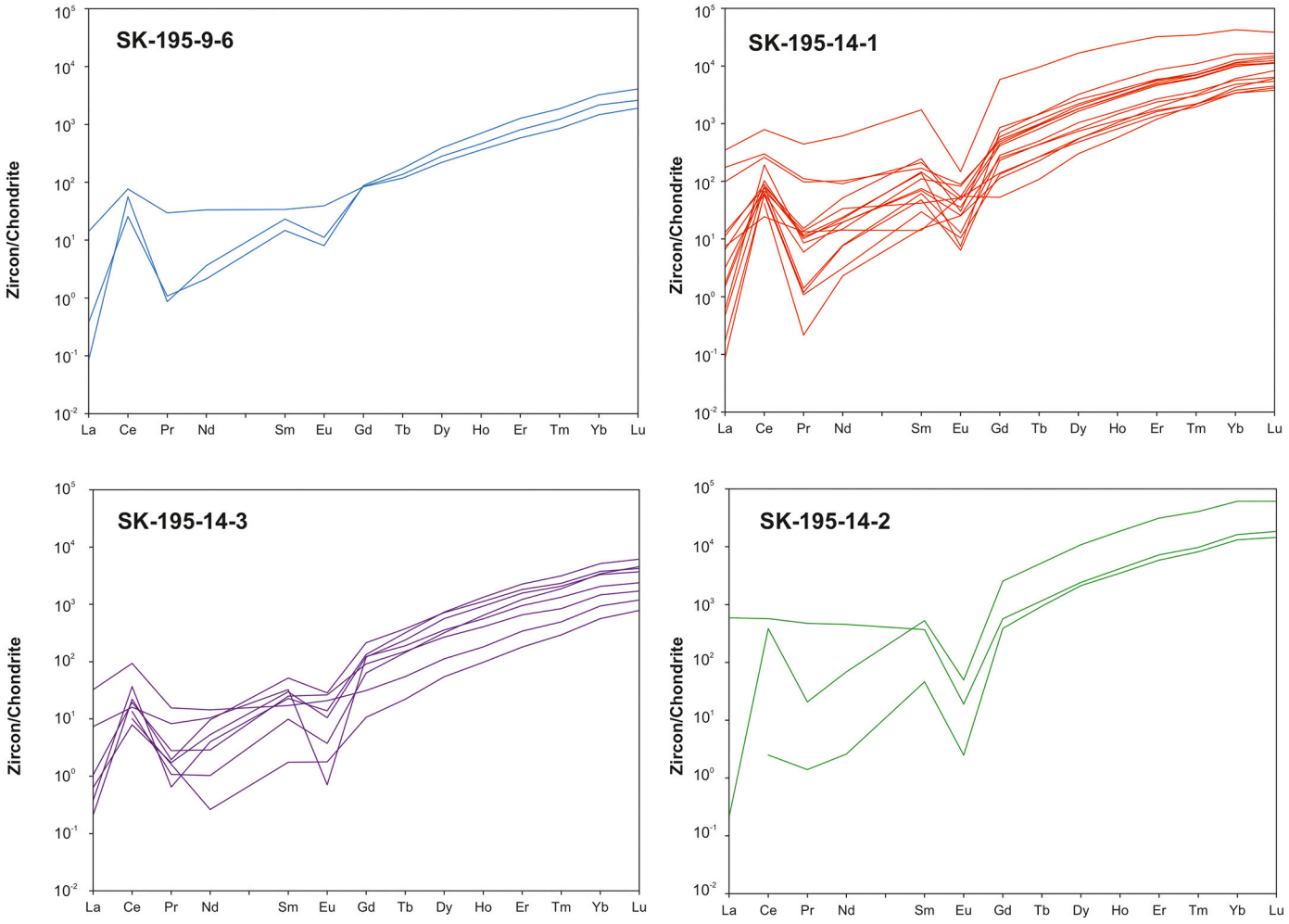

Fig. 6. Chondrite normalized REE patterns of zircon from the studied gabbros (normalization values are from Sun and McDonough, 1989).

conformity with that of N-MORB (Zr/Nb: 11–39) and recent oceanic primitive arc tholeiites (Zr/Nb: 9–87) thereby indicating depleted to enriched nature of the mantle source marked by interaction between asthenosphere and recycled lithospheric components (Pearce and Peate, 1995; Sun and McDonough, 1989). Therefore, the HFSE chemistry for the CIR gabbros is in compliance with the phenomenon of depleted mantle refertilization by recycled lithosphere. Ba/Nb and Ba/La ratios are reliable parameters to evaluate the fluid/water content and total slab-derived input in the mantle source respectively (Cervantes and Wallace, 2003; Saha et al., 2020; Yang et al., 2014). The Ba/Nb ratios for the studied samples ranging from 2.88–35.11 (avg. 16.72) corroborate a hydrated mantle source, while their Ba/La (6.54–38; avg. 20.47) ratios reflect overprinting of refractory, depleted signature of N-MORB type mantle by recycled metasomatized lithospheric components thereby augmenting pronounced geochemical heterogeneity of mantle beneath CIR.

Geochemical attributes for Carlsberg Ridge Basalts (CRB) and Central Indian Ridge Basalts (CIRB) yield crucial insights into their petrogenetic aspects in the context of the geochemical and tectonic evolution of the Indian Ocean mantle. The CRB and CIRB exhibit tholeiitic to transitional composition of precursor melts derived by high degree, shallow level partial melting of a spinel peridotite mantle source. They show E-MORB affinity with selective enrichment in incompatible trace elements. Higher values of Zr/Hf and Zr/Sm in conjunction with lower Nb/Ta ratio corroborate their origin from an enriched mantle source. Negative Nb anomalies with lower Nb/Y and Zr/Y conform to a non-plume origin of these basalts. Higher Zr/Nb and Th/Nb compared to OIB substantiate contributions from recycled subduction-processed components in the source mantle. Lower Nb/U values with higher Ba/Nb, and Ba/Th, Zr/Nb and Th/Nb compared to OIB and N-MORB attest to role of a metasomatized oceanic lithosphere that recycled into the depleted upper mantle attributing to the source heterogeneity. Sr—Nd isotopic signatures ($^{87}Sr/^{86}Sr$: 0.702668 to 0.702841 and $^{143}Nd/^{144}Nd$: 0.512972 to 0.513068) of CRB suggest a HIMU source component preserved in the northwest Indian Ocean Mid Oceanic Ridge mantle (Ray et al., 2013; Rehkamper and Hofmann, 1997; Saha et al., 2020). In conjunction with these, the geochemical data for the lower oceanic crust gabbros from Central Indian Ridge (CIR) suggest episodic recycling of ancient metasomatized continental lithosphere of Madagascan and Gondwana origin towards the Indian Ocean MOR mantle heterogeneity. The compositional diversity of the Indian Ocean MOR mantle can be translated in terms of periodic refertilization of depleted N-MORB type mantle through delamination and recycling of oceanic and continental lithosphere concurrent with Neoproterozoic-Paleozoic amalgamation and Jurassic dispersal of the Gondwana supercontinent respectively.

5.2. *Implications for zircon trace-REE chemistry and U—Pb ages*

Zircon, owing to its resistance to wide range of temperatures, pressures, and alteration mechanisms, provides a potential and robust time capsule recording magmatic, hydrothermal and metamorphic events that spatially and temporally punctuated the evolutionary history of the Earth as well as crust-mantle differentiation processes and crust building episodes. Fluid fluxes from subducted oceanic slab at convergent plate

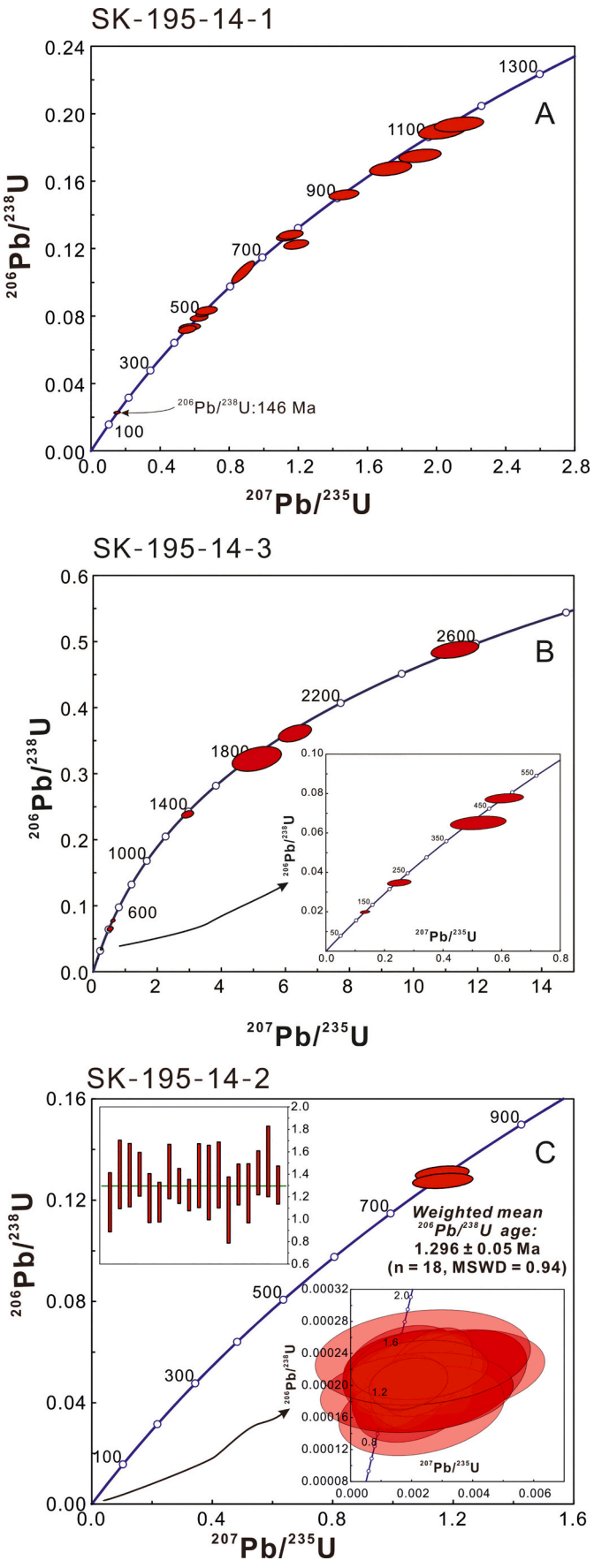

Fig. 7. Zircon U—Pb concordia plots for samples (A) SK-195-14-1 (B) SK-195-14-3 and (C) SK-195-14-2.

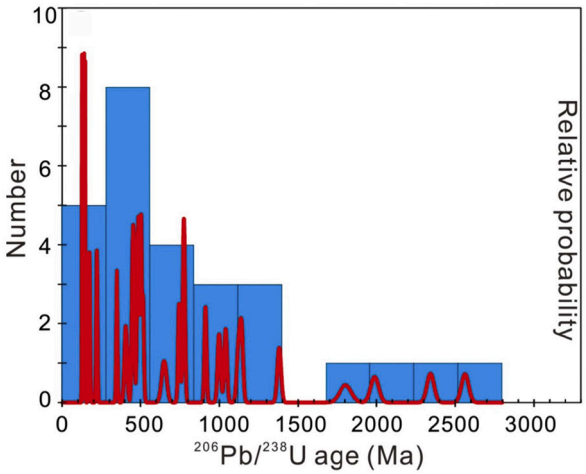

Fig. 8. Zircon U—Pb age data histograms with probability curves for samples SK-195-14-1, SK-195-14-3 and SK-195-14-2.

margins trigger melt-rock interactions, mantle wedge metasomatism and serpentinization. The fluid influx and subsequent metasomatic processes produce and enhance growth of zircon grains of magmatic and hydrothermal origin which in turn retain the memory of multiple orogenic cycles and evolutionary stages of mantle (Wang et al., 2019). Zircons of continental origin yield significant insights (Griffin et al., 2002; Grimes et al., 2007; Olierook et al., 2020) into the accretion, dispersal, assembly and recycling stages of crustal evolution. Continental zircons preserved in mantle derived rocks of ancient and modern oceanic environments provide clues to address recycling of ancient continental lithosphere, upper mantle heterogeneity and track the traces of paleo-continents lost and recycled in the mantle during collisional orogeny and terrane amalgamation.

The occurrences of zircons derived from old rocks have been discovered from the vicinity of present-day mid-oceanic ridges (Cheng et al., 2016; Schwartz et al., 2005). The zircons with ages 169 Ma, 330 Ma, 835 Ma and 1600 Ma, were obtained from different parts of the Mid-Atlantic Ridge while those with an age of 180 Ma was obtained from the Southwest Indian Ridge. Ages from both these ridges are inconsistent with seafloor spreading and therefore are crucial to understand the chemical geodynamic processes associated with crustal accretion in the mid-oceanic ridges. Geochronological studies including U—Pb dating and SHRIMP analyses of submarine gabbros exposed near the Kane fracture zone of the Mid Atlantic Ridge yield zircon ages in the range of 1600 Ma and 330 Ma (Pilot et al., 1998). The Proterozoic and Paleozoic ages of zircon grains recovered from the gabbros of the currently active Atlantic ridge system have been explained in terms of convective delamination and subsequent transportation of fragments of older continental lithosphere into the shallow mantle flanking the ridge axis concurrent with the opening of the Atlantic Ocean. An alternative hypothesis propounds a series of transform fault migration and ridge jump processes operative in response to the opening of the Atlantic that endorsed entrapment of older continental crust near the ridge axis within the Kane fracture zone (Pilot et al., 1998). Zircon U—Pb geochronology of tectonically uplifted lower crustal sections from mid oceanic ridge-rift systems has corroborated variable patterns of crustal accretion and melt transport mechanisms. U—Pb zircon ages from the Vema lithospheric sections on the MAR marginally vary between 13.75 and 13.25 Ma and this restricted range substantiates symmetrical accretion of oceanic crust by regular, ridge-centred shallow melt delivery at slow spreading ridges (Lissenberg et al., 2009). However, zircon U—Pb geochronological data for exposed lower crustal sections from Atlantis Bank on the SWIR and Atlantis Massif on the MAR reveal a protracted time span of crustal accretion dating back to 2.5 Ma. This

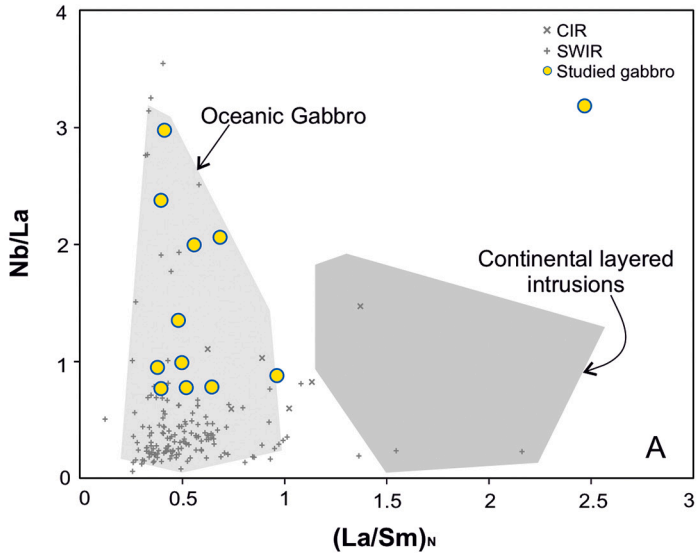

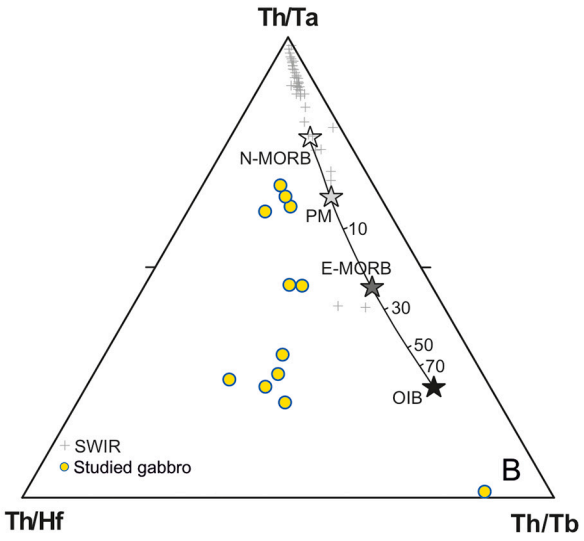

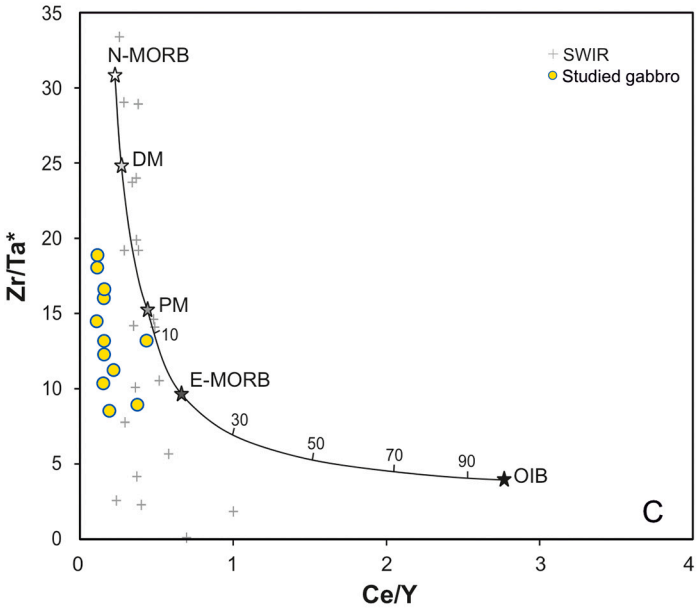

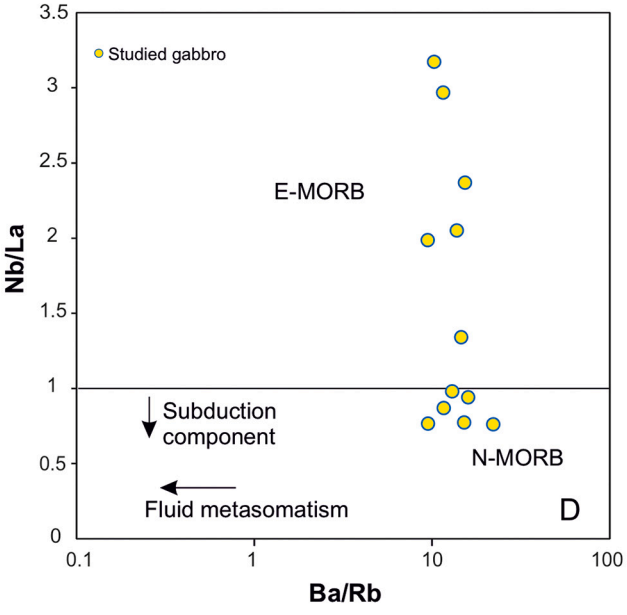

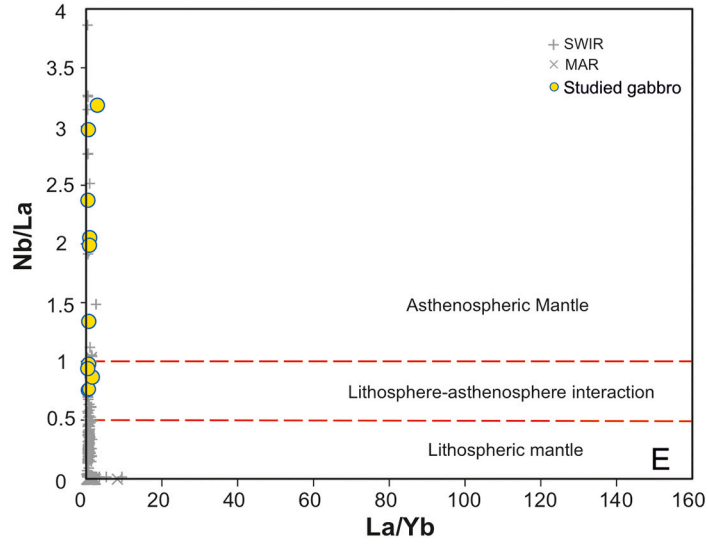

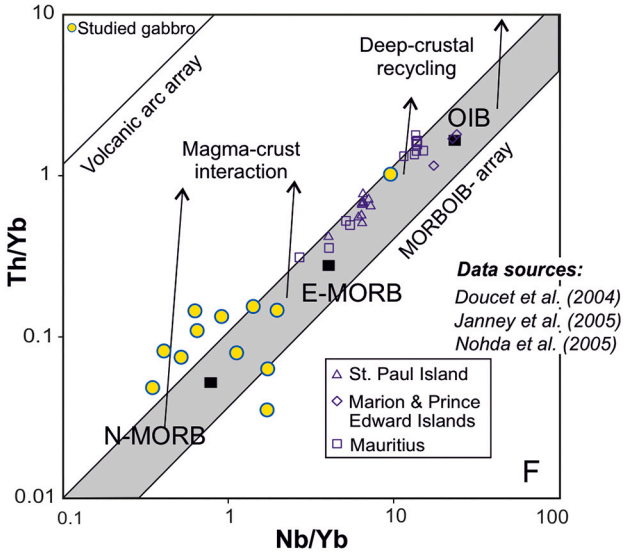

(caption on next page)

Fig. 9. Geochemical plots showing the mantle and tectonic characters of the studied gabbros, (A) plots of studied gabbros in $(La/Sm)_N$ vs Nb/La diagram reflecting their oceanic affinity, (B) plots of studied gabbros in Th/Ta-Th/Hf-Th/Tb diagram showing an enriched signature, (C) Zr/Ta* vs. Ce/Y discrimination diagram suggests an affinity towards *E*-MORB for the studied gabbros, (D) plots of studied gabbros in Ba/Rb vs. Nb/La diagram reflecting the influence of subduction-derived components for generation of parent magma, (E) low Nb/La and extremely low La/Yb ratios of the studied gabbros suggest an interaction of recycled subducted components at lithosphere-asthenosphere and asthenospheric mantle domain (after Abdel-Rahman and Nassar, 2004), (F) Th/Yb vs. Nb/Yb plots displaying a depleted to enriched character for the studied samples (Pearce, 2008).

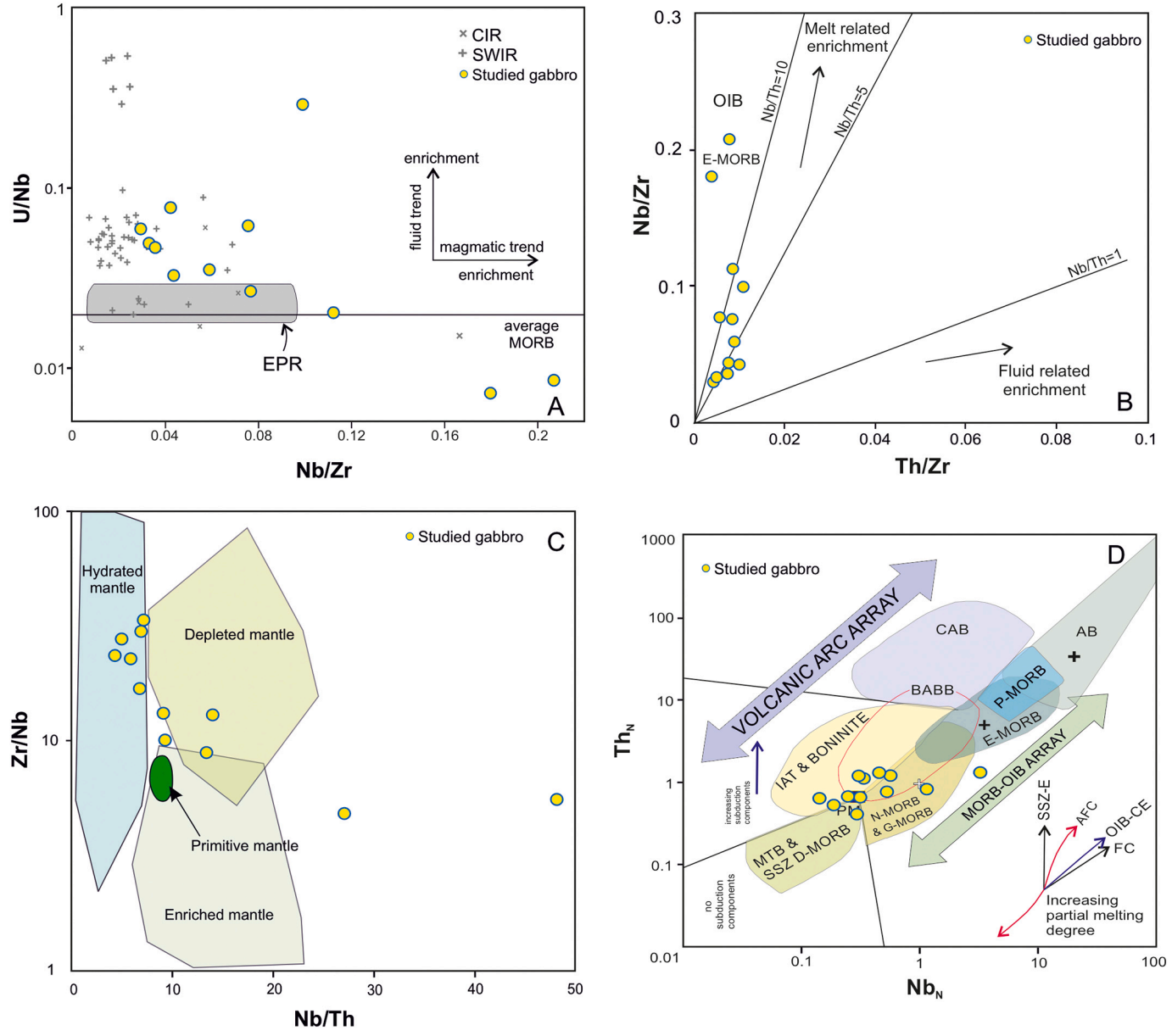

Fig. 10. Geochemical plots showing the melt characteristics of the studied gabbros, (A) plots of studied gabbros in Nb/Zr vs U/Nb diagram complying with enrichment of parent magma compared to depleted average N-MORB, (B) Nb/Zr vs. Th/Zr plot showing the studied in an array consistent with melt related enrichment of mantle through subduction process (after Zhao and Zhou, 2007) (C) Zr/Nb vs. Nb/Th plot reflecting role of depleted mantle for the generation of the studied rock (after Condie, 2015). A shifting from depleted mantle towards hydrated mantle source possibly fluxed by recycled subduction component (D) Th_N vs. Nb_N diagrams (after Saccani, 2015) showing the tectonic affinity for the studied samples.

record of prolonged crustal growth was predominantly governed by detachment faulting at asymmetrically spreading ridge segments that substantiated successive stages of magmatic intrusions, crystallization, uplift, melt replenishment and irregular patterns of plutonism at slow spreading ridges (Lissenberg et al., 2009). These observations collectively invoke symmetrical and asymmetrical patterns of crustal accretion at slow spreading ridges.

U—Pb geochronology of zircon grains from lower oceanic crust gabbros from CIR reveals a wide spectrum of ages ranging from 2525 Ma to 1.3 Ma (Fig. 8) that can be segregated into two groups based on their origin. The sub-rounded, xenocrystic zircons of 2525 Ma – 173 Ma reflect a continental inheritance, while the angular, autocrystic zircons of 154 Ma – 1.3 Ma corroborate an oceanic origin. Chondrite normalized zircon REE patterns (Fig. 11A) for the studied samples reflect a coherence with continental crust, detrital Hadean zircons and that of SWIR and MAR. On Yb vs U plot (Fig. 11B), zircons from gabbros of MAR and

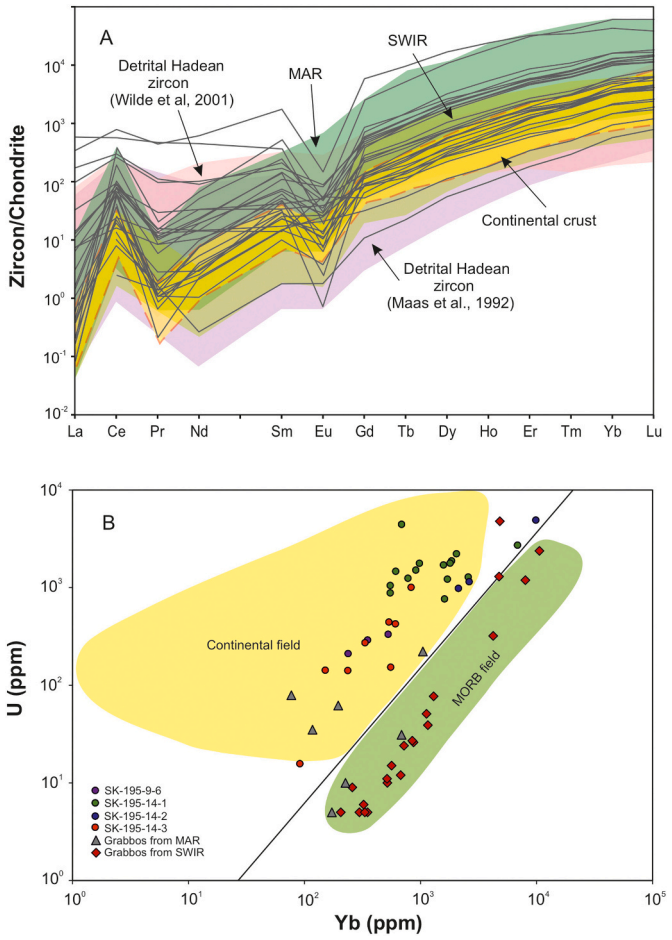

Fig. 11. (A) Chondrite normalized REE patterns of zircons from the studied gabbros in comparison with detrital Hadean zircon (Maas et al., 1992; Wilde et al., 2001), zircon data of Mid Atlantic Ridge and Southwest Indian Ridge, (B) Yb vs. U plots depicting the continental origin for the zircons of CIR gabbros, the fields for continental and MORB source are from Grimes et al., 2007

SWIR largely correspond to the MORB field thereby complying with a hydrothermal origin. However, 2525 Ma – 173 Ma zircons from the studied CIR gabbros distinctly corroborate a continental inheritance. This observation invokes recycling of ancient continental fragments into asthenospheric mantle and preservation of ancient continental signatures within oceanic gabbros. Our zircon data suggest multiple episodes of recycling of 2525 Ma – 173 Ma continental crust into asthenospheric mantle. Zircons of continental origin present in the lower oceanic crust gabbros of CIR build on the conjecture of trapped relics of older continental lithosphere that disintegrated, delaminated and swept into the asthenospheric mantle. The wide range of inherited zircons (2525 Ma–173 Ma) (Fig. 8) can be postulated in terms of (i) detachment faulting at slow spreading CIR augmenting irregular magma intrusions and asymmetric pattern of crustal accretion and (ii) multiple stages of recycling of ancient continental lithospheric fragments through convective delamination during opening and closing of ocean basins at ocean-continent transition zone associated with continental dispersal and amalgamation events respectively. The 154 Ma –1.3 Ma zircons owe their origin to magmatic processes operative during post Indian Ocean opening. It may be thus envisaged that these CIR gabbros inherited the characteristic geochemical signatures from the precursor melts derived from an upper mantle source that trapped fragments of older recycled continents. The oscillatory zoning discernible in majority of the studied zircon grains from CIR gabbros suggests a magmatic/igneous origin and the brighter rims around the magmatic core of the zircon grains correspond to overgrowth during younger magmatic events. Increasing magma temperature promotes higher Th contents relative to U resulting in higher Th/U ratios for zircons in mafic to intermediate rocks than in granitic rocks. Chondrite-normalized LREE enriched patterns with positive Ce and negative Pr and Eu anomalies and Th/U ratios (>0.5) for the older and younger zircon grains unambiguously distinguish them from hydrothermal zircons and reflect a magmatic origin (Rubatto, 2002; Santosh et al., 2009a, 2009b) thereby corroborating temporally distinct ancient and recent magmatic events concurrent with the pre and post Indian Ocean opening phases. The magmatic origin for 2525 Ma – 173 Ma zircons of continental inheritance can be translated in terms of their formation during magmatic processes involved in the genesis of older continental crust that subsequently got recycled. However, the 154 Ma–1.3 Ma zircons can be correlated with magmatism associated with oceanic crust formation during the opening of Indian Ocean after Gondwana dispersal. The zircon trace and REE geochemistry and U—Pb geochronology for the CIR gabbros collectively commensurate with distinct chemical heterogeneity of Indian Ocean MOR attained through multiple recycling of ancient lithospheric components during paleo-tectonic cycles.

5.3. *Multi-stage continental recycling and evolution of Indian MOR mantle*

The continental lithosphere principally comprises a mantle root or peridotitic keel that remains adhered to the crustal base and isolated from the underlying asthenospheric mantle both physically and chemically. Majority of the continental landmass of the Earth are underlain by thick, cold, melt-depleted mantle roots or rigid keels that form an integral part of the sub-continental lithospheric mantle (SCLM) (Perchuk et al., 2020). The distinct geochemical and isotopic composition of SCLM is attributed to melt generation and accretion processes concurrent with different thermotectonic events. The principal proponents for the origin of ancient SCLM include: (i) high degree melting of hot plume heads (>1650 °C), (ii) Accretion of ancient oceanic plateaus and arc lithosphere during subduction-accretion-collisional orogenic processes (Arndt et al., 2009; Capitanio et al., 2020). Subduction of oceanic and continental lithosphere, recycling of older crustal components are primary agents inducing compositional heterogeneity in the mantle. SCLM is refertilized and metasomatized by subduction-derived components at ocean-continent transition zones and delaminated into asthenospheric mantle during continent-continent collision. Recycling of ancient, metasomatized SCLM by delamination and downwelling during collisional orogenic processes has triggered episodic infusion of lithospheric mantle components into the asthenosphere (Hoernle et al., 2011; Rehkamper and Hofmann, 1997; Santosh et al., 2009a, 2009b). Thus, the chemical composition of a depleted asthenospheric mantle may be modified and overprinted by recycled subduction–derived lithospheric components with enriched signatures. The compositional diversity of the crust and mantle sections of oceanic lithosphere generated in divergent plate margin settings are attributed to magma plumbing, melt percolation, spreading rates, conductive cooling, crustal recycling and continental inputs. The typical depleted character of N-MORB mantle is variably replenished and modified by shallow contamination or deep mixing of crustal components carried by subducting oceanic lithosphere into asthenospheric mantle (Saha et al., 2020; Urann et al., 2020). The upwelling sub-ridge mantle asthenosphere acquires distinct enriched signatures through: (i) entrainment of ancient recycled metasomatized lithospheric fragments or (ii) mixing between N-MORB type depleted mantle and enriched recycled components of OIB mantle carried by plume-driven asthenospheric channels flows towards ridge segments. Subduction-driven crustal recycling and delamination of continental lithospheric mantle at ocean-continent transition zones collectively posit fulcrum mechanisms contributing to upper mantle heterogeneity and geochemical diversity. Subduction-driven delamination and convective downwelling have been proposed as two viable processes

that remove and entrain the continental lithosphere from margins of continents (Foley, 2008; Houseman and Molnar, 2001; Levander et al., 2014; Tao and O'connell, 1992). Seismic studies have revealed that thin lithosphere extends from continental margins at ocean-continent transition zone inwards to cratonic cores. Paleo-subduction events associated with ancient orogens might have viscously entrained and delaminated pre-conditioned SCLM from continental margins to asthenospheric mantle. The geochemical and isotopic signatures of the lower oceanic crust gabbros from CIR do not comply with OIB-type mantle component or geochemical signatures inherited from a mantle plume. Therefore, chemical composition of a depleted N-MORB type asthenospheric mantle beneath CIR may be replenished by recycling of ancient metasomatized lithospheric components with enriched signatures. The continental signature of the zircons from lower oceanic crust gabbros from CIR invokes the following possibilities: (i) ablative subduction; (ii) viscous entrainment, delamination and convective down welling of continental lithosphere into asthenospheric mantle; and (iii) subduction-driven recycling of ancient metasomatized continental lithosphere. Besides, ridge jump and fault migration processes associated with the opening of the Indian Ocean can also be considered as an alternative possibility that endorsed entrapment of older continental crust in the vicinity of CIR.

Zircon U—Pb data of CIR gabbros preserve a protracted record of multiple stages of continental recycling concurrent with ocean basin closure and continental amalgamation during Precambrian orogenic cycles and continent building episodes (Palin and Santosh, 2021; Santosh et al., 2009a, 2009b). The geochemical and geochronological signatures of the lower oceanic crust gabbros track recycled metasomatized continental lithosphere of Madagascan and Gondwana origin. Opening of an ocean basin at ocean-continent transition zone (OCTZ) involves rifting and upshearing of crust that collectively trigger delamination of continental lithosphere and upwelling of asthenospheric mantle lying beneath (Kay and Kay, 1993; Keen et al., 2018; Platt and Vissers, 1989). This convective removal leads to recycling and incorporation of continental lithospheric fragments into shallow sub-ridge mantle. The inception of the Indian Ocean Basin was in commensuration with the dispersal of Gondwanaland at ~167 Ma. The disintegration of the Gondwana supercontinent triggered rifting and subsequent delamination, convective removal of continental fragments and their recycling into the mantle asthenosphere. The preservation of 2525 Ma–173 Ma zircon grains of continental origin within oceanic gabbros of CIR can be correlated with the paleotectonic events associated with: (i) the closure of Mozambique ocean and Gondwana assembly at around 750 Ma, subduction-driven delamination, convective downwelling and recycling of older continental margin lithosphere into the mantle (Fig. 12A) and (ii) dispersal of Gondwanaland at ~167 Ma ensued by opening of Indian Ocean, delamination, convective removal and incorporation of older continental fragments into the upwelling mantle asthenosphere (Fig. 12B) in response to rifting and upshearing of crust and (iii) evolution of IORS with a chemical heterogeneous mantle beneath (Fig. 12C); detachment faulting at slow spreading CIR augmenting irregular magma intrusions and asymmetric pattern of crustal accretion. The continental lithospheric fragments that got recycled into the Indian Ocean MOR mantle carried traces of 2525 Ma – 173 Ma continental crust that was involved in several cycles of accretion, disintegration and amalgamation of ancient supercontinents (Palin and Santosh, 2021; Santosh et al., 2009a, 2009b) such as Ur (~ 3.1–2.4 Ga), Columbia (~1.8–1.3 Ga), Terra Borealis (~1.3–1.2 Ga), Rodinia (~1.1Ga – 750 Ma), Pannotia (633–573 Ma), Gondwana (550–180 Ma) (Nance et al., 2014; Rogers and Santosh, 2003). The 2525 Ma to 173 Ma zircons preserved in CIR gabbros suggest asymmetric accretion of crust extracted from a heterogeneous source mantle endowed with depleted and enriched components. It is thus envisaged that the spatio-temporal evolution of the Indian Ocean MOR mantle and its departure from depleted MAR mantle type signatures with characteristic geochemical and isotopic heterogeneity have been influenced by periodic

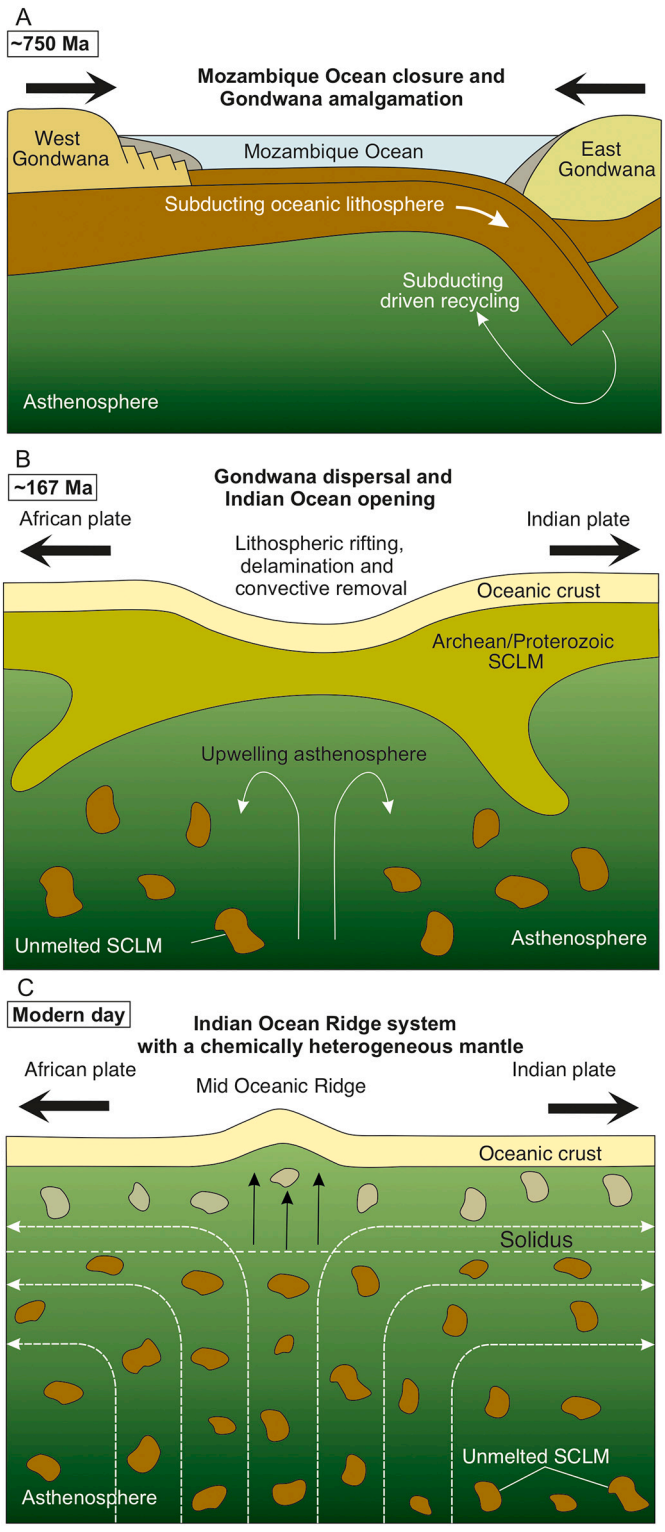

Fig. 12. Schematic illustration depicting the tectonic evolution of Indian MOR mantle, (A) the closure of Mozambique ocean and Gondwana assembly at ~750 Ma, subduction-driven delamination and recycling of older continental margin lithosphere into the mantle (modified after Saha et al., 2020), (B) dispersal of Gondwanaland at ~167 Ma and opening of Indian Ocean, delamination, convective removal and incorporation of older continental fragments into the upwelling mantle asthenosphere in response to rifting and upshearing of crust, (C) evolution of Indian Ocean Ridge System with a chemically heterogeneous mantle (modified after Hoernle et al., 2011).

delamination, convective downwelling and recycling of ancient metasomatized continental margin lithospheric fragments during closure of Mozambique Ocean-Gondwana assembly and opening of Indian Ocean-Gondwana dispersal.

6. Conclusions

- The CIR gabbros represent a section of the lower oceanic crust preserving distinct imprints of gravity settling and crystal segregation.
- The studied samples exhibit transitional geochemical characteristics with depleted to enriched mantle signatures.
- The trace element geochemistry of the CIR gabbros attests to the long-term compositional heterogeneity of the Indian Ocean MORB mantle derived through input of enriched, recycled lithospheric components into the depleted asthenospheric ridge mantle.
- Zircon U—Pb geochronology of the lower oceanic crust gabbros from CIR reveals their continental inheritance with a wide spectrum of ages ranging from 2525 Ma to 173 Ma thereby corroborating preserved evidence of ancient continental crust in oceanic gabbros.
- The 2525 Ma to 173 Ma inherited zircons from CIR gabbros are considered to record (i) multiple stages of recycling of continental lithosphere concurrent with the closure of Mozambique ocean and Gondwana assembly at around 750 Ma, and (ii) dispersal of Gondwana at ~167 Ma ensued by opening of the Indian Ocean.

Declaration of Competing Interest

None.

Acknowledgements

Authors are grateful to the Director, CSIR-National Institute of Oceanography for his encouragement, support and permission to publish this work. The authors sincerely acknowledge to all participating scientists and crew members of SK 195. The authors are thankful to Drs. K.A. KameshRaju, Ranadhir Mukhopadhyay and S.D.Iyer for sharing the samples. The authors acknowledge Prof. Michael Roden, Editor and two anonymous reviewers for their insightful comments. AS acknowledges the funding received from the Council of Scientific and Industrial Research (CSIR) and Ministry of Earth Sciences (MoES), Govt. of India under MLP 2017 and GAP 2175 respectively. AH acknowledges CSIR for Senior Research Fellowship, India (Grant no. RF83931). This is NIO's contribution No. 6791.

Appendix A. Supplementary data

Supplementary data to this article can be found online at https://doi.org/10.1016/j.lithos.2021.106424.

References

Abdel-Rahman, A.F.M., Nassar, P.E., 2004. Cenozoic volcanism in theMiddle East: petrogenesis of alkali basalts from northern Lebanon. Geol. Mag. 141, 545–563.
Agar, S.M., Casey, J.F., Kempton, P.D., Karson, J.A., 1997. Textural, geochemical, and isotopic variations in gabbroic shear zones from the MARK area 153, 99–122.
Arndt, N.T., Coltice, N., Helmstaedt, H., Gregoire, M., 2009. Origin of Archean subcontinental lithospheric mantle: some petrological constraints. Lithos 109, 61–71.
Ashwal, L.D., Wiedenbeck, M., Torsvik, T.H., 2017. Archaean zircons in Miocene oceanic hotspot rocks establish ancient continental crust beneath Mauritius. Nat. Commun. 8, 14086.
Bach, W., Alt, J.C., Niu, Y., Humphris, S.E., Erzinger, J., Dick, H.J., 2001. The geochemical consequences of late-stage low-grade alteration of lower ocean crust at the SW Indian Ridge: Results from ODP Hole 735B (Leg 176). Geochimica et Cosmochimica Acta 65, 3267–3287.
Barruol, G., Sigloch, K., Scholz, J.R., Mazzullo, A., Stutzmann, E., Montagner, J.P., Dyment, J., 2019. Large-scale flow of Indian Ocean asthenosphere driven by Réunion plume. Nat. Geosci. 12, 1043–1049.
Bonatti, E., Honnorez, J., Ferrara, G., 1971. Peridotite-gabbro-basalt complex from the equatorial Mid-Atlantic Ridge. Roy. Soc. London Philosoph. Transact. 268, 385–402.
Capitanio, F.A., Nebel, O., Cawood, P.A., 2020. Thermochemical lithosphere differentiation and the origin of cratonic mantle. Nature 588, 89–94.
Carlson, R.W., Ionov, D.A., 2019. Compositional characteristics of the MORB mantle and bulk silicate earth based on spinel peridotites from the Tariat Region, Mongolia. Geochim. Cosmochim. Acta 257, 206–223.
Casey, J.F., 1997. Comparison of major-and trace-element geochemistry of abyssal peridotites and mafic plutonic rocks with basalts from the MARK region of the Mid-Atlantic Ridge 153, 181–241.
Casey, J.F., Banerji, D., Zarian, P., Miller, D.J., 2007. Leg 179 synthesis: geochemistry, stratigraphy, and structure of gabbroic rocks drilled in ODP Hole 1105A, Southwest Indian Ridge 179, 1–125.
Cervantes, P., Wallace, P.J., 2003. Role of H_2O in subduction-zone magmatism: new insights from melt inclusions in high-Mg basalts from central Mexico. Geology 31 (3), 235–238.
Cheng, H., Zhou, H., Yang, Q., Zhang, L., Ji, F., Dick, H., 2016. Jurassic zircons from the Southwest Indian Ridge. Sci. Rep. 6, 1–9.
Condie, K., 2015. Changing tectonic settings through time: indiscriminate use of geochemical discriminant diagrams. Precambrian Res. 266, 587–591.
Coogan, L.A., O'Hara, M.J., 2015. MORB differentiation: in situ crystallization in replenished-tapped magma chambers. Geochim. Cosmochim. Acta 158, 147–161.
Coogan, L.A., Saunders, A.D., Kempton, P.D., Norry, M.J., 2000. Evidence from oceanic gabbros for porous melt migration within a crystal mush beneath the Mid-Atlantic Ridge. Geochem. Geophys. Geosyst. 1 (9).
Cortesogno, L., Gaggero, L., Zanetti, A., 2000. Rare earth and trace elements in igneous and high-temperature metamorphic minerals of oceanic gabbros (MARK area, Mid-Atlantic Ridge). Contribut. Mineral. Petrol. 139, 373–393.
Cox, K.G., Bell, J.D., Pankhurst, R.J., 1979. The Interpretation of Igneous Rocks, George Allen and Unwin (London, United Kingdom, 450 pp.).
D'Errico, M.E., Warren, J.M., Godard, M., 2016. Evidence for chemically heterogeneous Arctic mantle beneath the Gakkel Ridge. Geochim. Cosmochim. Acta 174, 291–312.
Dick, H.J., Lin, J., Schouten, H., 2003. An ultraslow-spreading class of ocean ridge. Nature 426 (6965), 405–412.
Drolia, R.K., DeMets, C., 2005. Deformation in the diffuse India-Capricorn-Somalia triple junction from a multibeam and magnetic survey of the northern Central Indian ridge, 3° S–10° S. Geochem. Geophys. Geosyst. 6 (9).
Drolia, R.K., Ghose, I., Subramanyam, A.S., Rao, M.M., Kessarkar, P., Murthy, K.S.R., 2000. Magnetic and bathymetric investigations over the Vema region of the Central Indian Ridge: tectonic implications. Mar. Geol. 167, 413–423.
Fisk, M.R., Duncan, R.A., Baxter, A.N., Greenough, J.D., Hargraves, R.B., Tatsumi, Y., 1989. Reunion hotspot magma chemistry over the past 65 my: results from Leg 115 of the Ocean Drilling Program. Geology 17, 934–937.
Fletcher, J.M., Stephens, C.J., Petersen, E.U., Skerl, L., 1997. Greenschist facies hydrothermal alteration of oceanic gabbros: A case study of element mobility and reaction paths 153, 389–398.
Foley, S.F., 2008. Rejuvenation and erosion of the cratonic lithosphere. Nat. Geosci. 1, 503–510.
Gale, A., Dalton, C.A., Langmuir, C.H., Su, Y., Schilling, J.G., 2013. The mean composition of ocean ridge basalts. Geochem. Geophys. Geosyst. 14 (3), 489–518.
Gale, A., Langmuir, C.H., Dalton, C.A., 2014. The global systematics of ocean ridge basalts and their origin. J. Petrol. 55, 1051–1082.
Griffin, W.L., Wang, Xiang, Jackson, S.E., Pearson, N.J., O'Reilly, Suzanne Y., Xu, Xisheng, Zhou, Xinmin, 2002. Zircon chemistry and magma mixing, SE China: in-situ analysis of Hf isotopes, Tonglu and Pingtan igneous complexes. Lithos 61, 237–269.
Grimes, C.B., John, B.E., Kelemen, P.B., Mazdab, F.K., Wooden, J.L., Cheadle, M.J., Schwartz, J.J., 2007. Trace element chemistry of zircons from oceanic crust: a method for distinguishing detrital zircon provenance. Geology 35, 643–646.
Hazra, A., Saha, A., Verencar, A., Satyanarayanan, M., Ganguly, S., Mahender, K., 2021. Refertilization of mantle peridotites from the Central Indian Ridge: response to a geodynamic transition. Lithosphere. https://doi.org/10.2113/2021/9706924.
Hekinian, R., Juteau, T., Gracia, E., Sichler, B., Sichel, S., Udintsev, G., Ligi, M., 2000. Submersible observations of equatorial atlantic mantle: the St. Paul Fracture Zone region. Marine Geophysical Researches 21, 529–560.
Hoernle, K., Hauff, F., Werner, R., van den Bogaard, P., Gibbons, A.D., Conrad, S., Müller, R.D., 2011. Origin of Indian Ocean Seamount Province by shallow recycling of continental lithosphere. Nat. Geosci. 4, 883–887.
Houseman, G., Molnar, P., 2001. Mechanisms of lithospheric rejuvenation associated with continental orogeny. Geol. Soc. Lond., Spec. Publ. 184, 13–38.
Ildefonse, B., Blackman, D.K., John, B.E., Ohara, Y., Miller, D.J., MacLeod, C.J., 2007. Oceanic core complexes and crustal accretion at slow-spreading ridges. Geology 35, 623–626.
Irvine, T.N.J., Baragar, W.R.A., 1971. A guide to the chemical classification of the common volcanic rocks. Can. J. Earth Sci. 8, 523–548.
Iyer, S.D., Ray, D., 2003. Structure, tectonic and petrology of mid-oceanic ridges and the Indian scenario. Curr. Sci. 277–289.
Kaczmarek, M.A., Müntener, O., Rubatto, D., 2008. Trace element chemistry and U–Pb dating of zircons from oceanic gabbros and their relationship with whole rock composition (Lanzo, Italian Alps). Contrib. Mineral. Petrol. 155, 295–312.
Kamesh Raju, K.A., Ramprasad, T., Subrahmanyam, C., 1997. Geophysical investigations over a segment of the Central Indian Ridge, Indian Ocean. Geo-Mar. Lett. 17, 195–201.
Kamesh Raju, K.A., Samudrala, K., Drolia, R.K., Amarnath, D., Ramachandran, R., Mudholkar, A., 2012. Segmentation and morphology of the Central Indian Ridge between 3 S and 11 S, Indian Ocean. Tectonophysics 554, 114–126.

Karson, J.A., Kelley, D.S., Fornari, D.J., Perfit, M.R., Shank, T.M., 2015. Discovering the Deep: A Photographic Atlas of the Seafloor and Ocean Crust. Cambridge University Press.
Kay, R.W., Kay, S.M., 1993. Delamination and delamination magmatism. Tectonophysics 219, 177–189.
Keen, C.E., Dickie, K., Dafoe, L.T., 2018. Structural evolution of the rifted margin off northern Labrador: the role of hyperextension and magmatism. Tectonics 37, 1955–1972.
Klein, E.M., Langmuir, C.H., 1987. Global correlations of ocean ridge basalt chemistry with axial depth and crustal thickness. J. Geophys. Res. 92, 8089–8115.
Kumagai, H., Dick, H.J., Kaneoka, I., 2003. Noble gas signatures of abyssal gabbros and peridotites at an Indian Ocean core complex. Geochem. Geophys. Geosys. 4, 9107.
Lambert, S., Laporte, D., Schiano, P., 2009. An experimental study of pyroxenite partial melts at 1 and 1.5 GPa: implications for the major-element composition of Mid-Ocean Ridge Basalts. Earth Planet. Sci. Lett. 288, 335–347.
Leuthold, J., Lissenberg, C.J., O'Driscoll, B., Karakas, O., Falloon, T., Klimentyeva, D.N., Ulmer, P., 2018. Partial melting of lower oceanic crust gabbro: constraints from poikilitic clinopyroxene primocrysts. Front. Earth Sci. 6, 15.
Levander, A., Bezada, M.J., Niu, F., Humphreys, E.D., Palomeras, I., Thurner, S.M., Miller, M.S., 2014. Subduction-driven recycling of continental margin lithosphere. Nature 515, 253–256.
Lin, J., Morgan, J.P., 1992. The spreading rate dependence of three-dimensional mid-ocean ridge gravity structure. Geophys. Res. Lett. 19, 13–16.
Lissenberg, C.J., Rioux, M., Shimizu, N., Bowring, S.A., Mével, C., 2009. Zircon dating of oceanic crustal accretion. Science 323 (5917), 1048–1050.
Lissenberg, C.J., MacLeod, C.J., Howard, K.A., Godard, M., 2013. Pervasive reactive melt migration through fast-spreading lower oceanic crust (Hess Deep, equatorial Pacific Ocean). Earth Planet. Sci. Lett. 361, 436–447.
Maas, R., Kinny, P.D., Williams, I.S., Froude, D.O., Compston, W., 1992. The Earth's oldest known crust: a geochronological and geochemical study of 3900–4200 Ma old detrital zircons from Mt. Narryer and Jack Hills, Western Australia. Geochim. Cosmochim. Acta 56, 1281–1300.
Macdonald, K.C., Fox, P.J., Perram, L.J., Eisen, M.F., Haymon, R.M., Miller, S.P., Shor, A. N., 1988. A new view of the mid-ocean ridge from the behaviour of ridge-axis discontinuities. Nature 335 (6187), 217–225.
Macdonald, K.C., Scheirer, D.S., Carbotte, S.M., 1991. Mid-ocean ridges: discontinuities, segments and giant cracks. Science 253, 986–994.
Mukhopadhyay, R., Iyer, S.D., Ray, D., Karisiddaiah, S.M., Drolia, R.K., 2016. Morphotectonic and petrological variations along the southern Central Indian Ridge. Int. J. Earth Sci. 105, 905–920.
Nance, R.D., Murphy, J.B., Santosh, M., 2014. The supercontinent cycle: a retrospective essay. Gondwana Res. 25, 4–29.
Olierook, H.K., Jourdan, F., Whittaker, J.M., Merle, R.E., Jiang, Q., Pourteau, A., Doucet, L.S., 2020. Timing and causes of the mid-Cretaceous global plate reorganization event. Earth Planet. Sci. Lett. 534, 116071.
Pagli, C., Wright, T.J., Ebinger, C.J., Yun, S.H., Cann, J.R., Barnie, T., Ayele, A., 2012. Shallow axial magma chamber at the slow-spreading Erta Ale Ridge. Nat. Geosci. 5, 284–288.
Pagli, C., Mazzarini, F., Keir, D., Rivalta, E., Rooney, T.O., 2015. Introduction: anatomy of rifting: tectonics and magmatism in continental rifts, oceanic spreading centers, and transforms. Geosphere 11, 1256–1261.
Palin, R.M., Santosh, M., 2021. Plate tectonics: what, where, why, and when? Gondwana Res. https://doi.org/10.1016/j.gr.2020.11.001.
Patriat, P., Achache, J., 1984. India–Eurasia collision chronology has implications for crustal shortening and driving mechanism of plates. Nature 311, 615–621.
Pearce, J.A., 2008. Geochemical fingerprinting of oceanic basalts with applications to ophiolite classification and the search for Archean oceanic crust. Lithos 100, 14–48.
Pearce, J.A., Peate, D.W., 1995. Tectonic implications of the composition of volcanic arc magmas. Annu. Rev. Earth Planet. Sci. 23, 251–286.
Perchuk, A.L., Gerya, T.V., Zakharov, V.S., Griffin, W.L., 2020. Building cratonic keels in Precambrian plate tectonics. Nature 586, 395–401.
Pilot, J., Werner, C.D., Haubrich, F., Baumann, N., 1998. Palaeozoic and proterozoic zircons from the Mid-Atlantic ridge. Nature 393, 676–679.
Platt, J.P., Vissers, R.L.M., 1989. Extensional collapse of thickened continental lithosphere: a working hypothesis for the Alboran Sea and Gibraltar arc. Geology 17, 540–543.
Radhakrishna, M., Verma, R.K., 2000. Seismotectonics of the Central Indian Ridge, western Indian Ocean. J. Geol. Soc. India 55, 515–527.
Ray, D., Misra, S., Banerjee, R., 2013. Geochemical variability of MORBs along slow to intermediate spreading Carlsberg-Central Indian Ridge, Indian Ocean. J. Asian Earth Sci. 70, 125–141.
Rehkamper, M., Hofmann, A.W., 1997. Recycled ocean crust and sediment in Indian Ocean MORB. Earth Planet. Sci. Lett. 147, 93–106.
Rogers, J.J., Santosh, M., 2003. Supercontinents in Earth history. Gondwana Res. 6, 357–368.
Rubatto, D., 2002. Zircon trace element geochemistry: partitioning with garnet and the link between U–Pb ages and metamorphism. Chem. Geol. 184, 123–138.
Saccani, E., 2015. A new method of discriminating different types of post-archeanophiolitic basalts and their tectonic significance using Th-Nb and Ce- Dy-Yb systematics. Geosci. Front. 6, 48–501.
Safonova, I.Y., Simonov, V.A., Buslov, M.M., Ota, T., Maruyama, S., 2008. Neoproterozoic basalts of the Paleo-Asian Ocean (Kurai accretionary zone, Gorny Altai, Russia): geochemistry, petrogenesis, and geodynamics. Russ. Geol. Geophys. 49, 254–271.
Saha, A., Sensarma, S., Hazra, A., Ganguly, S., Peketi, A., Doley, B., Mudholkar, A.V., 2020. Imprints of ancient recycled oceanic lithosphere in heterogeneous Indian Ocean mantle: evidence from petrogenesis of Carlsberg ridge basalts from Northwest Indian Ocean. Gondwana Res. 86, 60–82.
Santosh, M., Maruyama, S., Sato, K., 2009a. Anatomy of a Cambrian suture in Gondwana: Pacific-type orogeny in southern India? Gondwana Res. 16, 321–341.
Santosh, M., Wan, Y., Liu, D., Chunyan, D., Li, J., 2009b. Anatomy of zircons from an ultrahot orogen: the amalgamation of the North China craton within the supercontinent Columbia. J. Geol. 117, 429–443.
Saunders, A.D., Norry, M.J., Tarney, J., 1988. Origin of MORB and chemically-depleted mantle reservoirs: trace element constraints. J. Petrol. 1, 415–445.
Schwartz, J.J., John, B.E., Cheadle, M.J., Miranda, E.A., Grimes, C.B., Wooden, J.L., Dick, H.J., 2005. Dating the growth of oceanic crust at a slow-spreading ridge. Science 310, 654–657.
Scott, J.M., Hodgkinson, A., Palin, J.M., Waight, T.E., Van der Meer, Q.H.A., Cooper, A. F., 2014. Ancient melt depletion overprinted by young carbonatitic metasomatism in the New Zealand lithospheric mantle. Contrib. Mineral. Petrol. 167, 963.
Scott, J.M., Liu, J., Pearson, D.G., Harris, G.A., Czertowicz, T.A., Woodland, S.J., Luth, R. W., 2019. Continent stabilisation by lateral accretion of subduction zone-processed depleted mantle residues; insights from Zealandia. Earth Planet. Sci. Lett. 507, 175–186.
Sun, S.S., McDonough, W.F., 1989. Chemical and isotopic systematics of oceanic basalts: implications for mantle composition and processes. Geol. Soc. Lond., Spec. Publ. 42, 313–345.
Tao, W.C., O'connell, R.J., 1992. Ablative subduction: a two-sided alternative to the conventional subduction model. J. Geophys. Res. 97 (B6), 8877–8904.
Tolstoy, M., Harding, A.J., Orcutt, J.A., 1993. Crustal thickness on the Mid-Atlantic Ridge: Bull's-eye gravity anomalies and focused accretion. Science 262, 726–729.
Urann, B.M., Dick, H.J.B., Parnell-Turner, R., Casey, J.F., 2020. Recycled arc mantle recovered from the Mid-Atlantic Ridge. Nat. Commun. 11, 1–9.
Wang, J., Santosh, M., Li, S., Kim, S.W., 2019. Magmatic and hydrothermal zircon growth during multiple orogenic cycles in an evolving mantle wedge. Geosci. Front. 10, 439–452.
White, R.S., Minshull, T.A., Bickle, M.J., Robinson, C.J., 2001. Melt generation at very slow-spreading oceanic ridges: constraints from geochemical and geophysical data. J. Petrol. 42, 1171–1196.
Wilde, S.A., Valley, J.W., Peck, W.H., Graham, C.M., 2001. Evidence from detrital zircons for the existence of continental crust and oceans on the Earth 4.4 Gyr ago. Nature 409 (6817), 175–178.
Wilson, M., 1989. Igneous Petrogenesis. Unwin Hyman, London (466 pp.).
Yang, A.Y., Zhou, M.F., Zhao, T.P., Deng, X.G., Qi, L., Xu, J.F., 2014. Chalcophile elemental compositions of MORBs from the ultraslow-spreading Southwest Indian Ridge and controls of lithospheric structure on S-saturated differentiation. Chem. Geol. 382, 1–13.
Yi, S.B., Oh, C.W., Pak, S.J., Kim, J., Moon, J.W., 2014. Geochemistry and petrogenesis of mafic-ultramafic rocks from the Central Indian Ridge, latitude 8–17 S: denudation of mantle harzburgites and gabbroic rocks and compositional variation of basalts. Int. Geol. Rev. 56, 1691–1719.
Zhang, G.L., Luo, Q., Zhao, J., Jackson, M.G., Guo, L.S., Zhong, L.F., 2018. Geochemical nature of sub-ridge mantle and opening dynamics of the South China Sea. Earth Planet. Sci. Lett. 489, 145–155.
Zhao, J.H., Zhou, M.F., 2007. Geochemistry of Neoproterozoic mafic intrusions in the Panzhihua district (Sichuan Province, SW China): implications for subduction-related metasomatism in the upper mantle. Precambrian Res. 152, 27–47.